

Beam dynamics corrections to the Run-1 measurement of the muon anomalous magnetic moment at Fermilab

T. Albahri,³⁸ A. Anastasi,^{11, a} K. Badgley,⁷ S. Baeßler,^{45, b} I. Bailey,^{19, c} V. A. Baranov,¹⁷ E. Barlas-Yucel,³⁶ T. Barrett,⁶ F. Bedeschi,¹¹ M. Berz,²⁰ M. Bhattacharya,⁴² H. P. Binney,⁴⁶ P. Bloom,²¹ J. Bono,⁷ E. Bottalico,^{11, 31} T. Bowcock,³⁸ G. Cantatore,^{13, 33} R. M. Carey,² B. C. K. Casey,⁷ D. Cauz,^{34, 8} R. Chakraborty,³⁷ S. P. Chang,^{18, 5} A. Chapelain,⁶ S. Charity,⁷ R. Chislett,³⁵ J. Choi,⁵ Z. Chu,^{25, d} T. E. Chupp,⁴¹ S. Corrodi,¹ L. Cotrozzi,^{11, 31} J. D. Crnkovic,^{3, 36, 42} S. Dabagov,^{9, e} P. T. Debevec,³⁶ S. Di Falco,¹¹ P. Di Meo,¹⁰ G. Di Sciascio,¹² R. Di Stefano,^{10, 29} A. Driutti,^{34, 13, 37} V. N. Duginov,¹⁷ M. Eads,²² J. Esquivel,⁷ M. Farooq,⁴¹ R. Fatemi,³⁷ C. Ferrari,^{11, 14} M. Fertl,^{46, 16} A. Fiedler,²² A. T. Fienberg,⁴⁶ A. Fioretti,^{11, 14} D. Flay,⁴⁰ E. Frlež,⁴⁵ N. S. Froemming,^{46, 22} J. Fry,⁴⁵ C. Gabbanini,^{11, 14} M. D. Galati,^{11, 31} S. Ganguly,^{36, 7} A. Garcia,⁴⁶ J. George,⁴⁰ L. K. Gibbons,⁶ A. Gioiosa,^{28, 11} K. L. Giovanetti,¹⁵ P. Girotti,^{11, 31} W. Gohn,³⁷ T. Gorringer,³⁷ J. Grange,^{1, 41} S. Grant,³⁵ F. Gray,²³ S. Haciomeroglu,⁵ T. Halewood-Leagas,³⁸ D. Hampai,⁹ F. Han,³⁷ J. Hempstead,⁴⁶ A. T. Herrod,^{38, c} D. W. Hertzog,⁴⁶ G. Hesketh,³⁵ A. Hibbert,³⁸ Z. Hodge,⁴⁶ J. L. Holzbauer,⁴² K. W. Hong,⁴⁵ R. Hong,^{1, 37} M. Iacovacci,^{10, 30} M. Incagli,¹¹ P. Kammel,⁴⁶ M. Kargiantoulakis,⁷ M. Karuza,^{13, 43} J. Kaspar,⁴⁶ D. Kawall,⁴⁰ L. Kelton,³⁷ A. Keshavarzi,³⁹ D. Kessler,⁴⁰ K. S. Khaw,^{26, 25, 46, d} Z. Khechadorian,⁶ N. V. Khomutov,¹⁷ B. Kiburg,⁷ M. Kiburg,^{7, 21} O. Kim,^{18, 5} Y. I. Kim,⁵ B. King,^{38, a} N. Kinnaird,² M. Korostelev,^{19, c} E. Kraegeloh,⁴¹ N. A. Kuchinskiy,¹⁷ K. R. Labe,⁶ J. LaBounty,⁴⁶ M. Lancaster,³⁹ M. J. Lee,⁵ S. Lee,⁵ B. Li,^{25, 1, d} D. Li,^{25, f} L. Li,^{25, d} I. Logashenko,^{4, g} A. Lorente Campos,³⁷ A. Lucà,⁷ G. Lukicov,³⁵ A. Lusiani,^{11, 24} A. L. Lyon,⁷ B. MacCoy,⁴⁶ R. Madrak,⁷ K. Makino,²⁰ F. Marignetti,^{10, 29} S. Mastroianni,¹⁰ J. P. Miller,² S. Miozzi,¹² W. M. Morse,³ J. Mott,^{2, 7} A. Nath,^{10, 30} D. Newton,^{38, h} H. Nguyen,⁷ R. Osofsky,⁴⁶ S. Park,⁵ G. Pauletta,^{34, 8} G. M. Piacentino,^{28, 12} R. N. Pilato,^{11, 31} K. T. Pitts,³⁶ B. Plaster,³⁷ D. Počanić,⁴⁵ N. Pohlman,²² C. C. Polly,⁷ J. Price,³⁸ B. Quinn,⁴² N. Raha,¹¹ S. Ramachandran,¹ E. Ramberg,⁷ J. L. Ritchie,⁴⁴ B. L. Roberts,² D. L. Rubin,⁶ L. Santi,^{34, 8} D. Sathyan,² C. Schlesier,³⁶ A. Schreckenberger,^{44, 2, 36} Y. K. Semertzidis,^{5, 18} M. W. Smith,^{46, 11} M. Sorbara,^{12, 32} D. Stöckinger,²⁷ J. Stapleton,⁷ C. Stoughton,⁷ D. Stratakis,⁷ T. Stuttard,³⁵ H. E. Swanson,⁴⁶ G. Sweetmore,³⁹ D. A. Sweigart,⁶ M. J. Syphers,^{22, 7} D. A. Tarazona,²⁰ T. Teubner,³⁸ A. E. Tewsley-Booth,⁴¹ K. Thomson,³⁸ V. Tishchenko,³ N. H. Tran,² W. Turner,³⁸ E. Valetov,^{20, 19, 26, c} D. Vasilkova,³⁵ G. Venanzoni,¹¹ T. Walton,⁷ A. Weisskopf,²⁰ L. Welty-Rieger,⁷ P. Winter,¹ A. Wolski,^{38, c} and W. Wu⁴²

(The Muon $g - 2$ Collaboration)

¹Argonne National Laboratory, Lemont, Illinois, USA

²Boston University, Boston, Massachusetts, USA

³Brookhaven National Laboratory, Upton, New York, USA

⁴Budker Institute of Nuclear Physics, Novosibirsk, Russia

⁵Center for Axion and Precision Physics (CAPP) / Institute for Basic Science (IBS), Daejeon, Republic of Korea

⁶Cornell University, Ithaca, New York, USA

⁷Fermi National Accelerator Laboratory, Batavia, Illinois, USA

⁸INFN Gruppo Collegato di Udine, Sezione di Trieste, Udine, Italy

⁹INFN, Laboratori Nazionali di Frascati, Frascati, Italy

¹⁰INFN, Sezione di Napoli, Naples, Italy

¹¹INFN, Sezione di Pisa, Pisa, Italy

¹²INFN, Sezione di Roma Tor Vergata, Rome, Italy

¹³INFN, Sezione di Trieste, Trieste, Italy

¹⁴Istituto Nazionale di Ottica - Consiglio Nazionale delle Ricerche, Pisa, Italy

¹⁵Department of Physics and Astronomy, James Madison University, Harrisonburg, Virginia, USA

¹⁶Institute of Physics and Cluster of Excellence PRISMA+,

Johannes Gutenberg University Mainz, Mainz, Germany

¹⁷Joint Institute for Nuclear Research, Dubna, Russia

¹⁸Department of Physics, Korea Advanced Institute of Science and Technology (KAIST), Daejeon, Republic of Korea

¹⁹Lancaster University, Lancaster, United Kingdom

²⁰Michigan State University, East Lansing, Michigan, USA

²¹North Central College, Naperville, Illinois, USA

²²Northern Illinois University, DeKalb, Illinois, USA

²³Regis University, Denver, Colorado, USA

²⁴Scuola Normale Superiore, Pisa, Italy

²⁵School of Physics and Astronomy, Shanghai Jiao Tong University, Shanghai, China

²⁶Tsung-Dao Lee Institute, Shanghai Jiao Tong University, Shanghai, China

²⁷Institut für Kern- und Teilchenphysik, Technische Universität Dresden, Dresden, Germany

- ²⁸ *Università del Molise, Campobasso, Italy*
²⁹ *Università di Cassino e del Lazio Meridionale, Cassino, Italy*
³⁰ *Università di Napoli, Naples, Italy*
³¹ *Università di Pisa, Pisa, Italy*
³² *Università di Roma Tor Vergata, Rome, Italy*
³³ *Università di Trieste, Trieste, Italy*
³⁴ *Università di Udine, Udine, Italy*
³⁵ *Department of Physics and Astronomy, University College London, London, United Kingdom*
³⁶ *University of Illinois at Urbana-Champaign, Urbana, Illinois, USA*
³⁷ *University of Kentucky, Lexington, Kentucky, USA*
³⁸ *University of Liverpool, Liverpool, United Kingdom*
³⁹ *Department of Physics and Astronomy, University of Manchester, Manchester, United Kingdom*
⁴⁰ *Department of Physics, University of Massachusetts, Amherst, Massachusetts, USA*
⁴¹ *University of Michigan, Ann Arbor, Michigan, USA*
⁴² *University of Mississippi, University, Mississippi, USA*
⁴³ *University of Rijeka, Rijeka, Croatia*
⁴⁴ *Department of Physics, University of Texas at Austin, Austin, Texas, USA*
⁴⁵ *University of Virginia, Charlottesville, Virginia, USA*
⁴⁶ *University of Washington, Seattle, Washington, USA*
(Dated: April 8, 2021)

This paper presents the beam dynamics systematic corrections and their uncertainties for the Run-1 data set of the Fermilab Muon $g-2$ Experiment. Two corrections to the measured muon precession frequency ω_a^m are associated with well-known effects owing to the use of electrostatic quadrupole (ESQ) vertical focusing in the storage ring. An average vertically oriented motional magnetic field is felt by relativistic muons passing transversely through the radial electric field components created by the ESQ system. The correction depends on the stored momentum distribution and the tunes of the ring, which has relatively weak vertical focusing. Vertical betatron motions imply that the muons do not orbit the ring in a plane exactly orthogonal to the vertical magnetic field direction. A correction is necessary to account for an average pitch angle associated with their trajectories. A third small correction is necessary because muons that escape the ring during the storage time are slightly biased in initial spin phase compared to the parent distribution. Finally, because two high-voltage resistors in the ESQ network had longer than designed RC time constants, the vertical and horizontal centroids and envelopes of the stored muon beam drifted slightly, but coherently, during each storage ring fill. This led to the discovery of an important phase-acceptance relationship that requires a correction. The sum of the corrections to ω_a^m is 0.50 ± 0.09 ppm; the uncertainty is small compared to the 0.43 ppm statistical precision of ω_a^m .

CONTENTS

I. Introduction	3	E. Magnetic field considerations	9
II. Experimental Details	4	F. Beam dynamics simulation tools	9
A. Experimental Principle	4	1. GEANT4-based <code>gm2ringsim</code>	9
B. The Run-1 data set	5	2. COSY INFINITY	10
C. From muon injection to muon storage	6	3. BMAD	10
D. Instrumentation employed to study the muon beam and decay positrons	7	III. Determination of the Stored Muon Momentum Distribution	11
		A. Momentum-Time Correlation	12
		B. Frequency domain fast rotation analysis: Fourier method	12
		C. Time domain fast rotation analysis: debunching method	12
		D. The radial distributions for Run-1	13
		IV. Electric Field Correction, C_e	13
		A. Measuring the muon radial distribution and calculating C_e	14
		V. Pitch Correction, C_p	15
		A. Measuring the muon vertical distribution and calculating C_p	15

^a Deceased.

^b Also at Oak Ridge National Laboratory.

^c Also at The Cockcroft Institute of Accelerator Science and Technology.

^d Also at Shanghai Key Laboratory for Particle Physics and Cosmology; also at Key Lab for Particle Physics, Astrophysics and Cosmology (MOE).

^e Also at Lebedev Physical Institute and NRNU MEPhI.

^f Also at Shenzhen Technology University.

^g Also at Novosibirsk State University.

^h Also at The Cockcroft Institute of Accelerator Science and Technology; Deceased.

VI. Dynamic Effects Owing To Time-changing Fields	16
A. Changes to the betatron frequencies	16
B. Changes to the muon spatial distribution	18
VII. Muon Loss Correction, C_{ml}	19
A. Muon loss rate determination	20
B. Phase-momentum correlation determination	20
C. Lost-muon momentum correlation determination	21
D. Value of the muon loss correction	22
VIII. Correction for Muon Distribution Time-Dependence, C_{pa}	23
A. Measurement of the time-changing muon distribution	25
B. Estimation of beam distribution around the storage ring	25
C. Phase-acceptance correction: results and uncertainty evaluation	26
IX. Conclusion	27
A. Summary of Run-1 net corrections to ω_a^m	28
X. Acknowledgments	28
A. Electric Quadrupole Nonlinearity	28
1. Path length correction owing to curved geometry	29
2. Effect from the intrinsic quadrupole nonlinearity	30
B. E -field and pitch corrections explored numerically	30
C. Maps for the phase-acceptance correction	32
1. Acceptance maps	32
2. Phase and Asymmetry maps	33
D. Precession Fit Function	33
References	34

I. INTRODUCTION

The measurement of the muon magnetic anomaly¹ $a_\mu \equiv (g_\mu - 2)/2$, where g_μ is the factor describing the relationship of the muon magnetic moment to its spin, has undergone significant development since the late 1960s when the idea of using a magnetic storage ring for the measurement was first introduced [1]. Two storage ring experiments at CERN [1, 2] and the Brookhaven National

Laboratory (BNL) Experiment (E821) [3] have increasingly refined the technique, leading to a determination of a_μ to a precision of 0.54 ppm [3]. These experiments determine a_μ by measuring the muon spin precession frequency relative to the momentum vector while a muon beam is confined in a storage ring. In an ideal case with muons orbiting in a horizontal plane with a uniform vertical magnetic field, the anomalous precession frequency ω_a is given by the difference between the spin (s) and cyclotron (c) frequencies, $\omega_a = \omega_s - \omega_c$. The observable ω_a is proportional to a_μ .

A highly precise determination of a_μ is motivated by the fact that the standard model (SM) prediction [4] is known to 0.37 ppm and thus a direct comparison with the experiment serves as an excellent and sensitive test of its completeness. The E821 a_μ measurement [3] is larger than the SM prediction; the level of significance is 3.7 standard deviations (σ). This difference can be interpreted as a hint of new physics or an indication of unaccounted-for systematic errors in the experiment or theory. The Fermilab Muon $g-2$ Experiment (E989) is designed to test the validity of the BNL result and to go further by improving on the experimental precision.

The principle of an a_μ measurement in a storage ring lies in the expression

$$a_\mu = \frac{\omega_a}{\tilde{\omega}'_p(T_r)} \frac{\mu'_p(T_r)}{\mu_e(H)} \frac{\mu_e(H)}{\mu_e} \frac{m_\mu}{m_e} \frac{g_e}{2}, \quad (1)$$

where the experiment measures the two quantities in the ratio $\omega_a/\tilde{\omega}'_p(T_r)$, and the fundamental constants – the proton-to-electron magnetic moment ratio [5], the QED factor $\mu_e(H)/\mu_e$ [6], the muon-to-electron mass ratio [6, 7], and the electron g_e factor [8] – are obtained from external measurements and calculations.

Reference [9] – a companion to this paper – reports the first results from the analysis of the Run-1 data collected in 2018:

$$a_\mu(\text{FNAL}) = 116\,592\,040(54) \times 10^{-11} \text{ (0.46 ppm)}.$$

The statistical (0.43 ppm), systematic (0.15 ppm), and external fundamental constant (0.03 ppm) uncertainties are combined in quadrature. The result is in good agreement with the BNL result and, when the two measurements are combined and compared to the SM, the significance of the difference between experiment and theory rises to 4.2σ . In order to obtain this result, a number of beam dynamics effects had to be accounted for in the analysis. This paper reports the methods used to quantify the impact of these effects and their uncertainties. These effects were part of a larger analysis, which can be summarized briefly as follows.

In Eq. 1, term $\tilde{\omega}'_p(T_r)$ represents the magnetic field sampled by the muons and measured using pulsed proton NMR. The magnitude of the field is calibrated in terms of the equivalent precession frequency $\omega'_p(T_r)$ of a proton shielded in a spherical sample of water at a reference temperature $T_r = 34.7^\circ\text{C}$. The detailed analysis of

¹ a_μ is a scalar quantity and thus not technically the “anomalous magnetic moment” that is ubiquitous in the literature.

the magnetic field determination for this experiment is reported in a second companion paper [10].

The anomalous precession frequency ω_a in the numerator of Eq. 1 is extracted from a fit to the time and energy spectrum of positrons, which encodes a modulation of its intensity at the anomalous precession frequency. Importantly, the frequency extracted by fitting the data is the *measured* quantity ω_a^m , and not the desired quantity ω_a needed to obtain a_μ in Eq. 1. Details of the measured precession frequency ω_a^m analysis, including statistical and systematic uncertainties, are reported in the final companion paper to this report [11].

The muons in the experiment do not orbit in a perfectly horizontal plane in a homogeneous vertical magnetic field. An electrostatic quadrupole (ESQ) system is required to provide relatively weak vertical focusing. The resulting presence of an electric field and vertical betatron oscillations, as well as muons lost during the measurement period, and a faulty ESQ component that led to a time-dependent optical lattice necessitate “beam dynamics” corrections that must be applied to ω_a^m in order to obtain ω_a , the quantity needed to determine the magnetic anomaly.

Two corrections are a result of a physical reduction in the spin precession frequency of the muons. The electric-field correction C_e is a result of muons traveling orthogonally through the radial electric field from the ESQ system and experiencing a motional vertical magnetic field. The pitch correction C_p compensates for the vertical betatron motion that causes, on average, a slightly non-orthogonal relation between the muon momentum and the vertically aligned magnetic field. While these were known from previous experiments, two additional corrections must be made to compensate for a dynamic change to the stored muon ensemble’s average spin phase during each injection cycle of muons into the ring. The C_{ml} correction is associated with muons lost during storage that have a slightly different spin phase compared to those that remain stored. Finally, because two high-voltage resistors in the ESQ network had longer than designed RC time constants, the vertical and horizontal centroids and envelopes of the stored muon beam drifted slightly, but coherently, during each storage ring fill. This led to the discovery of an important phase-acceptance relationship that requires a correction C_{pa} . The four corrections are applied in a linear combination² to ω_a^m ,

$$\omega_a \approx \omega_a^m (1 + C_e + C_p + C_{ml} + C_{pa}) . \quad (2)$$

The total shift to the measured ω_a^m value is (+0.50 ± 0.09) ppm. Although these small corrections are all at the sub-ppm level, the net correction exceeds the statistical uncertainty on ω_a^m , and thus the corrections must be scrutinized carefully and their uncertainties determined

² Cross terms between corrections are neglected here which is more than sufficient.

precisely. A thorough discussion is presented in this paper.

Section II includes background information on the formal experimental principle, Run-1 data set characteristics, injection and storage information, and descriptions of the experimental instrumentation, magnetic field, and the simulation tools. The electric-field correction is evaluated using the stored muon momentum distribution that is obtained via a data-driven procedure described in Section III. The C_e correction and its uncertainty can be found in Section IV. The pitch correction C_p is discussed in Section V.

The time-dependent nature of the detected oscillation phase which compels the final two corrections was exacerbated during Run-1 due to damage to two out of 32 high-voltage resistors in the ESQ charging system. Section VI examines the consequences of this unexpected configuration for the time-dependent electric quadrupole field and the dynamics of the stored beam. Section VII discusses how this slow change of the steering field leads to larger than expected muon losses and evaluates the resulting correction C_{ml} due to a correlation between muon momentum and initial average spin phase. Section VIII describes the phase-acceptance correction C_{pa} that is introduced because the muon average spatial distribution of the beam drifts during storage as a result of the same ESQ resistor issue.

Finally, we summarize and conclude in Sec. IX and provide four Appendices covering details of electric field and pitch corrections, the generation of phase, asymmetry, and acceptance maps needed for the C_{pa} correction, and a typical fitting function used to determine ω_a^m .

II. EXPERIMENTAL DETAILS

A. Experimental Principle

Polarized positive muons are injected into a 14.2-m-diameter storage ring having a highly uniform ~ 1.45 T vertical magnetic field; each individual injection sequence is termed a “fill”. For muons of momentum p_μ orbiting in a horizontal plane that is perpendicular to a perfectly uniform magnetic field ($\vec{B} \cdot \vec{p}_\mu = 0$), the magnitude of the cyclotron frequency is $\omega_c = |q|B/m\gamma$, where q , m , and γ are the muon charge, mass, and Lorentz factor respectively. The torque on the magnetic moment, together with the Thomas precession, rotates the muon spin at the frequency $\omega_s = g_\mu|q|B/2m + (1 - \gamma)|q|B/\gamma m$ [12]. The anomalous precession frequency ω_a can then be described as the difference

$$\omega_a \equiv \omega_s - \omega_c = \left(\frac{g_\mu - 2}{2} \right) \frac{|q|B}{m} = a_\mu \frac{|q|B}{m} . \quad (3)$$

Because of parity violation in the μ^+ weak decay, positrons are emitted with an energy and an angular distribution that are each highly correlated to the muon spin

direction in its rest frame. Ignoring effects from beam dynamics, the detectors that are distributed uniformly around the inside of the storage ring see a positron count rate versus time-in-fill t and positron energy E with the following functional form:

$$N(t, E) = N_0(E)e^{-t/\gamma\tau_\mu} \{1 + A(E) \cos[\omega_a t + \varphi_0(E)]\}. \quad (4)$$

The normalization, time-dilated muon lifetime, asymmetry, anomalous precession frequency, and phase constant at the time of injection are represented in Eq. 4 by $N_0(E)$, $\gamma\tau_\mu$, $A(E)$, ω_a and $\varphi_0(E)$, respectively. The energy dependence of N_0 and A has its origin in the Lorentz-boosted muon decay (Michel) spectrum; the actual values depend on the detector acceptance. The asymmetry also depends on the muon ensemble average polarization magnitude \mathcal{P}_μ , which is $\approx 95\%$ in this experiment. In practice, ω_a is determined from a fit to a positron time spectrum having a range of positron energies. The detector design is optimized to accept higher-energy positrons for which the figure-of-merit NA^2 is maximized.

We emphasize that, throughout this paper, the variable φ_0 represents the phase constant in the time-dependent phase angle of the cosine in Eq. 4. Its value is determined by the fitting procedure and need not, and cannot, be determined with sufficient precision *a priori* to the fit of the spin precession data sample. The phase constant φ_0 is dependent on the stored muon momentum p_μ , the decay positron energy E , and the transverse decay coordinates³ (x, y) inside the storage ring. The N_0 and A terms in Eq. 4 are also functions of the same quantities, but they couple much more weakly to ω_a^m . The physical interpretation of these dependencies of the phase constant and their implications to systematic uncertainties in the determination of ω_a are most important in the determination of the C_{ml} and C_{pa} correction factors discussed in Sec. VII and VIII, respectively.

The relevant observable for the anomalous precession frequency is the oscillation in the quantity $\hat{\beta} \cdot \vec{S}$, where \vec{S} is the spin vector of the muon. Following the Thomas-BMT equation [13] for spin and the Lorentz equation for momentum, one observes that, in the presence of an electric field \vec{E} ,

$$\frac{d(\hat{\beta} \cdot \vec{S})}{dt} = -\frac{q}{m} \vec{S}_T \cdot \left[a_\mu \hat{\beta} \times \vec{B} + \beta \left(a_\mu - \frac{1}{\gamma^2 - 1} \right) \frac{\vec{E}}{c} \right], \quad (5)$$

where \vec{S}_T is the component of \vec{S} perpendicular to $\hat{\beta}$ and we have ignored a possible term owing to a nonzero muon electric dipole moment, which has been determined to be negligible [14]. This expression corresponds exactly to the muon spin precession in the ring. The electric field

term in Eq. 5 vanishes for muons having the “magic” momentum $p_0 = 3.094 \text{ GeV}/c$ ($\gamma \sim 29.3$). The experiment is therefore designed around injection and storage of muons centered on p_0 .

B. The Run-1 data set

The muon delivery and experimental apparatus were commissioned from June 2017 to March 2018. The Run-1 data-taking period began on March 26, 2018 and concluded on July 7, 2018. The data sets in this analysis comprise 14.13 M muon fills. Approximately 5000 muons are stored in each fill, at an average of 11.4 fills per second.

Vertical focusing in the storage ring is achieved using a suite of ESQ plates that occupy 43% of the ring circumference. The field index n , responsible for the relatively weak focusing in the vertical direction, is defined by

$$n = \frac{R_0}{vB_0} \frac{\partial E_y}{\partial y}, \quad (6)$$

where R_0 is the central orbit radius, v is the muon velocity, B_0 is the magnetic field, and the gradient in the effective vertical electric field is determined from the plate voltages and geometry. Four distinct data sets, referred to hereafter as 1a, 1b, 1c, 1d, have been separately analyzed corresponding to four different combinations of kicker magnet and ESQ voltages (see Table I). The separate analyses of these data sets yield consistent results for a_μ . The 18.3 kV ($n = 0.108$) and 20.4 kV ($n = 0.120$) values were chosen to avoid storage ring betatron resonance conditions that would lead to large muon losses.

Data Set	$\delta\omega_a^m$ (stat) ppb	ESQ kV	Effective Field Index	Kicker kV
Run-1a	1206	18.3	0.108	130
Run-1b	1024	20.4	0.120	137
Run-1c	825	20.4	0.120	130
Run-1d	676 [†]	18.3	0.107	125

TABLE I. The Run-1 data set characteristics: the columns indicate the statistical uncertainty of ω_a^m based on the asymmetry-weighted analysis method [11]; the demand ESQ voltage; the measured field index n which is affected by the damaged ESQ resistors (Section II C); and, the typical kicker strength in kV used to deflect the incoming beam into the storage volume.

[†] The precession fit start time for Run-1d was delayed to 50 μs , in contrast to 30 μs for the other data groups.

The different field indices lead to differing beam frequencies since the horizontal and vertical betatron tunes for a uniform set of quadrupole fields that occupy the full azimuth of the storage ring are given by

$$\nu_x = \sqrt{1 - n} \quad \text{and} \quad \nu_y = \sqrt{n}, \quad (7)$$

³ Our coordinate system is with respect to the center of the storage volume at radius R_0 , with x or r radially outward, y vertically up, and ϕ increasing clockwise when viewed from above.

with corresponding betatron frequencies

$$\omega_x = \omega_c \sqrt{1-n} \quad \text{and} \quad \omega_y = \omega_c \sqrt{n}. \quad (8)$$

These expressions are sufficiently accurate for our purposes. Calculations of the frequencies for the different field indices are shown in Table II. Coherent radial and vertical betatron oscillations of the centroid and width of the stored beam are driven by a combination of the mismatch between the beamline admittance and the storage ring acceptance, the intrinsic divergence of the incoming beam, and the strength of the storage ring kicker system. The radial coherent betatron motion of the muon ensemble introduces an oscillatory time-dependence to the N_0 , A , and φ_0 terms in Eq. 4. Since $\omega_x > \omega_c/2$, the observed frequency at each detector is the aliased frequency $\omega_{\text{CBO}} = \omega_c - \omega_x$. These coherent betatron oscillations (CBO) occur inside the storage volume, but become imprinted on the positron count spectrum $N(t)$ because of the radial dependence of the detector acceptance. The radial mean of the muon distribution is modulated at frequency ω_{CBO} and the radial width (RMS) at $2\omega_{\text{CBO}}$, and also at ω_{CBO} if the stored beam is not centered in the aperture. A smaller, but similar effect exists for the vertical oscillations, where ω_y is observed without aliasing, but the width oscillations at $2\omega_y$ are aliased to $\omega_{\text{VW}} = \omega_c - 2\omega_y$. Due to the symmetric nature of the vertical detector acceptance, the ω_{VW} effect is stronger than that from ω_y . The calculated values of ω_{CBO} and ω_{VW} are also presented in Table II.

These effects impact N_0 , A , and φ_0 , and are accounted for by additional terms in the fitted positron decay time spectrum (see Appendix D and Ref. [11]). The field indices have been chosen such that the modulations do not couple strongly to ω_a^m . If the ESQ system does not maintain stable voltages within a fill, ω_{CBO} and ω_{VW} vary as a function of time-in-fill, which was the case in Run-1, but fixed thereafter.

Physical Frequency	Calculated Expression	Frequency (rad/ μs)	
		$n = 0.108$	$n = 0.120$
ω_c	v/R_0	42.15	42.15
ω_x	$\sqrt{1-n}\omega_c$	39.81	39.54
ω_y	$\sqrt{n}\omega_c$	13.85	14.60
ω_{CBO}	$\omega_c - \omega_x$	2.34	2.61
ω_{VW}	$\omega_c - 2\omega_y$	14.45	12.95
ω_a	$ea_\mu B/m$	1.44	1.44

TABLE II. Characteristic frequencies for the Run-1 field indices. The physical frequencies are described in the text. All values are calculated from the simple expressions shown and are similar to the measured values.

C. From muon injection to muon storage

Muons from the Fermilab accelerator complex are created as follows. Bunches of 8-GeV protons strike a target

in the AP0 building of the Muon Campus [15]. The average number of protons incident on the target per muon fill was 9.84×10^{11} . Positive 3.1 GeV/c particles are extracted and transported through the 279-m-long M2/M3 FODO beamline⁴. Roughly 80% of the pions decay to muons in this beamline section, which is optimized to produce a muon beam with an average longitudinal polarization of approximately 95%. The particles then enter the 505 m-circumference Delivery Ring, where they are allowed to circulate for four full turns. The accompanying 3.1 GeV/c protons from the target station lag behind the faster muons and are swept out by an in-ring fast-kicker magnet. The purified and polarized muon bunch is then directed along the M4 and M5 beamlines and into the storage ring. The net 2463 m path length from the target to the storage ring reduces the initial pion intensity by a factor 1.5×10^6 , an important feature that eliminates the hadronically induced flash at injection, which was challenging in the E821 experiment [3].

Sixteen individual bunches of muons are injected every 1.4 s cycle in two sequences of eight with 10 ms separation, and 267 ms between the start of each sequence. The average temporal intensity distribution of muons at the entrance to the storage ring is shown in dashed red in Fig. 1. The shape of this intensity-time distribution varies slightly for each of the eight fills in a group.

Figure 2 shows a plan view of the main components and detectors in the storage ring. Not shown for clarity in the figure is the ‘‘C-shaped’’ superconducting storage ring magnet [16]. It was transported from BNL to Fermilab, rebuilt and reshimmed by our collaboration to a roughly threefold improved uniformity. The NMR probes used to measure the absolute and relative magnetic field are all new, but they closely follow designs developed for E821 [17]. The superconducting inflector magnet [18], the ESQ hardware [19], and the vacuum chambers are used ‘‘as is’’ from E821. The ESQ power supply system and its controls, the entire storage ring kicker system, and all detectors and associated electronics were custom designed for E989.

The storage ring is designed to accept muons in a narrow momentum range around p_0 ; however, the incoming beam has a comparatively wide momentum spread of $\pm 1.6\%$ and no upstream dispersive focus. Only a few percent of the particles are stored with a momentum width less than $\pm 0.15\%$. The muon bunch enters the ring through a nearly field-free corridor – 18 mm-wide \times 56 mm-high \times 1700 mm-long – provided by the superconducting inflector magnet [18]. Three kicker stations (K1, K2, K3) create a vertical magnetic field that opposes the main storage ring field and thus deflects the muons passing through them outward by ~ 10 mrad. Ideally, this transient field is turned off before the muons complete a full turn in about 149 ns. A challenge in this experiment

⁴ Alternating focusing and defocusing quadrupole magnets

is creating such a transient magnetic kick and timing it with respect to each muon bunch. Figure 1 also shows a sample of the measured kicker induced magnetic field overlaid with the muon bunch. The kicker pulse shape and magnetic field strength are discussed later in the context of the stored muon momentum distribution within the ring. The kick is not uniform across the full temporal extent of the incoming muon bunch, a fact that impacts the total storage efficiency and the momentum distribution of the stored beam.

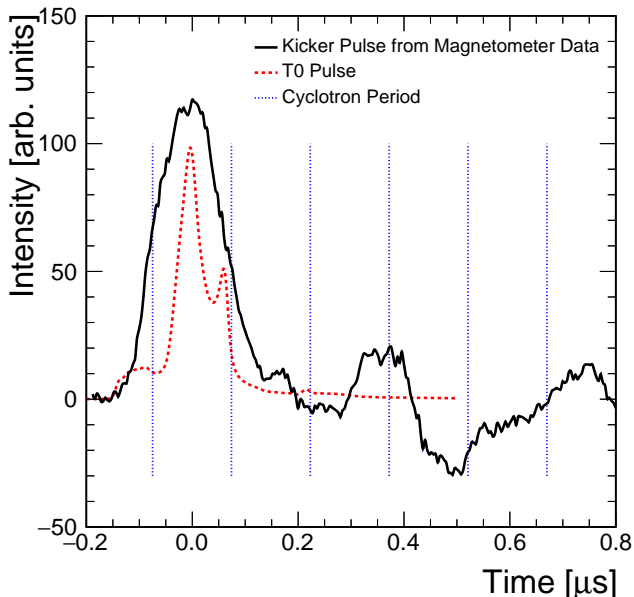


FIG. 1. The solid black trace represents the shape of the kicker magnetic field. The ringing is owing to an unavoidable impedance mismatch. The dashed red trace represents the average injected muon bunch temporal intensity distribution as measured by the T0 detector. The vertical dotted lines are separated by the 149 ns cyclotron period. The overlay between kicker and beam shapes shows that not all entering muons experience the same magnetic deflection. It is clear from the ringing that muons experience multiple kicks, both inward and outward.

Four ESQ stations are symmetrically placed around the ring. Each consists of a long (L) and a short (S) section spanning 26° and 13° , respectively. Thus Q1 in Fig. 2 has sections Q1L and Q1S, each with four plates that are connected to power supplies through individual high-voltage resistors. The plates are raised from ground to operating voltage prior to each fill with RC charging time constants of $\sim 5 \mu\text{s}$. They are returned to ground at the end of the $700 \mu\text{s}$ long fill. Plates are charged using either 1-step or 2-step power supplies. Those plates connected to the 2-step supplies rise to a preset voltage that is set to be $\sim 5 - 7 \text{ kV}$ below their final designed voltage. After a programmable delay of approximately $7 \mu\text{s}$, they are raised to the full setpoint voltage. This procedure, known as scraping, initially displaces the beam vertically and horizontally with respect to the central closed or-

bit. When a muon's horizontal and vertical oscillations conspire to exceed a 45 mm-radius with respect to the quadrupole center, it will likely strike a collimator, scatter and lose energy. Such muons leave the storage volume in a few turns. When the voltages are symmetrized, the muon distribution relaxes back to the nominal center, where muon losses are minimized. This scraping process is designed to be completed by $30 \mu\text{s}$ after injection, before the nominal measurement start time.

The charging traces of the ESQ plates for the Run-1 configuration are shown in Fig. 3. As noted, 30 of 32 charging profiles follow the nominal and ideal pattern as shown in the solid black and dotted red traces for the 1-step and 2-step supplies, respectively. However, following the completion of Run-1 data taking, it was discovered that two resistors had dynamically changed their resistances when high voltage was applied. The resulting traces, measured after the data-taking period, are shown in dotted blue and solid orange in Fig. 3. These resistors were connected to the upper and lower plates of the Q1L system. Because they are asymmetric and did not rise to their proper voltage prior to the fit start time, they introduced a perturbation to the stored muon spatial distribution vs. time-in-fill. As will be evident in later sections, this was likely responsible for the larger-than-expected rate of lost muons, and it created a time-dependent phase shift from the correlations of decay position to average phase owing to the detector acceptance. The changing voltages within the measurement time also led to a change in the storage ring tune values, the consequence of which is a dependence of the CBO frequency vs. time-in-fill. The $\omega_{\text{CBO}}(t)$ variation is well-measured and included in the fits that determine the anomalous precession frequency. These damaged resistors were replaced prior to Run-2.

The temporal bunch structure of the injected muon beam does not fill the storage ring uniformly. Observing how this bunch spreads out owing to the finite momentum distribution is central to determining the stored muon momentum distribution (see Sec III). For Run-1a, 1b, and 1c, the measuring period to determine ω_a^m begins $30 \mu\text{s}$ after injection, an optimization of minimizing systematic uncertainties and maximizing statistical significance. During Run-1d, the damaged resistors deteriorated further, causing greater perturbations to the stability of the muon storage distribution at early times in the fill. A delayed fit start time of $50 \mu\text{s}$ is used for this data set, allowing the quadrupole voltages to more closely reach to their target values.

D. Instrumentation employed to study the muon beam and decay positrons

The detectors employed to measure the incoming and stored muon bunches are the T0, IBMS, Calorimeter, and Tracker systems. They are orientated as shown in Fig. 2. Their signals are recorded using deadtimeless digitizers

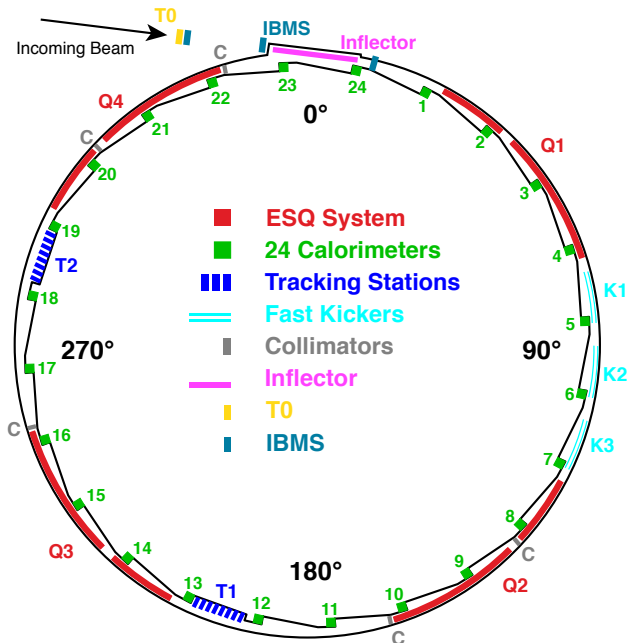


FIG. 2. Plan view of the $g-2$ storage ring vacuum chamber and instrumentation highlighting the important components discussed in this paper. The beam enters through a field-free corridor provided by the inflector magnet. Three kicker stations operate in concert to deflect the beam onto a stable orbit during the first turn. Four quadrupole stations, each consisting of a short and long section, provide vertical containment. The T0 and IBMS detectors monitor the injected beam intensity, time profile, and spatial distribution.

and saved fill by fill for offline processing. The injected muon bunch first passes through the T0 and IBMS detectors, located at the entrance to the storage ring. They are used to measure the intensity of the incoming beam, its temporal and spatial profile, and to establish the average entrance time of the bunch on a fill by fill basis, which is required for the analysis of the momentum distribution as discussed in Sec. III. The T0 detector is a 1.0-mm thick plastic scintillator with dual PMT readout. The two IBMS detectors each consist of a horizontal and vertical array of 16 0.5 mm-diameter scintillating fibers.

Twenty-four electromagnetic calorimeters are positioned symmetrically around the inside radius of the storage ring, adjacent to the storage volume, but outside of the vacuum chamber, see Fig. 2. The scallop profile in the chamber allows decay positrons that curl towards smaller radii to exit through a thin, nearly perpendicular aluminum window before striking a detector. Each calorimeter station consists of 54 lead-fluoride Cherenkov crystals read out individually on the downstream side by large-area SiPMs [20, 21]. The signals are continuously digitized at 800 mega-samples per second. The precise time alignment of the 1296 crystals and the system gain stability is enabled using a laser system as described in Ref. [22]. Reconstruction of positron showers in the

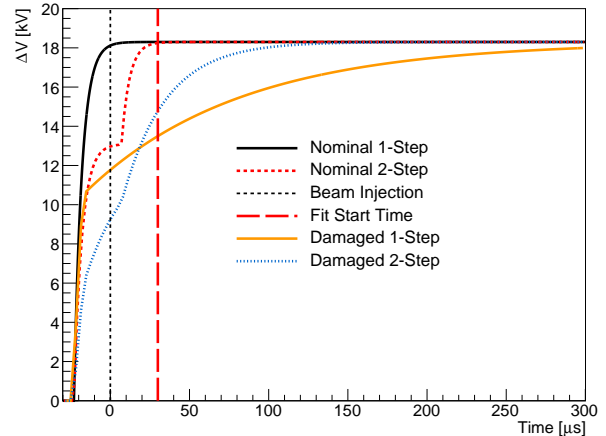


FIG. 3. Charging profiles for the 30 nominal quadrupole plates driven by either 1-step (black) or 2-step (dotted red) power supplies. The two damaged resistors (solid orange and dotted blue), connected to the same 1- and 2-step power supplies, exhibit markedly different charging profiles during the data fitting period. The vertical dotted black line at time $t = 0$ represents the arrival time of the muons in the storage ring. The vertical dashed red line at $30 \mu\text{s}$ indicates the time at which the precession data fits begin. The resistors deteriorated slightly for Run-1d and the precession fit start time was delayed to $50 \mu\text{s}$ to compensate for the longer time charging profiles.

calorimeter crystals yield energy, time-of-hit, and impact position. The coincidence of signals in three consecutive calorimeters, each depositing an energy typical of a minimum ionizing muon of about 170 MeV, is used to identify muon losses and measure the loss rate vs. time-in-fill.

The straw tracker systems are located at approximately 180° and 270° with respect to beam injection. They reside within the vacuum chamber in the scallop region just upstream of a calorimeter, but outside of the muon storage volume. Both stations consist of eight modules, each made of 128 5-mm diameter straws oriented at $\pm 7.5^\circ$ with respect to the vertical. They are used to track the decay positrons with the intention of tracing the decay trajectory back to its point of tangency inside the storage volume, a good proxy for the decay position of the parent muon. High quality tracks are selected to construct distributions of the beam position at the tracker locations. These measurements are corrected for momentum-dependent detector resolution and the non-uniform acceptance of the detector. The magnitudes of the corrections are estimated using the `gm2ringsim` package described below. These trackers are critical to all beam dynamics topics discussed in this paper. They provide the muon profile vs. time, which is used to determine key storage properties, such as the betatron horizontal and vertical frequencies, their time-dependence owing to the damaged resistor influence, and the vertical distribution for the pitch correction.

E. Magnetic field considerations

The highly uniform magnetic field amplitude $B = |\vec{B}|$ within the storage volume allows for the extraction of the spatial field structure with NMR probe measurements [10]. The magnet iron poles and iron shims are precisely aligned in order to minimize the RMS variations of the multipole terms as a function of azimuth. The reduction of the field nonuniformities improves several systematic uncertainties in the measurement of the magnetic field, including the extraction of the frequency from the NMR probe measurements and the uncertainty due to limited knowledge of the probe positions. Priority is given to the reduction of the lowest-order multipoles that couple to the moments of the muon beam. Surface correction coils on the surfaces of the pole pieces are utilized to reduce the azimuthally averaged field multipole strengths. Typically, the azimuthally averaged multipoles are reduced to below ~ 1 ppm, as shown in Table III.

The main measurement uncertainties in the mapping of the field, detailed in Ref. [10], stem from motional effects of the mapping device and the probe positions. Because of the overall field uniformity, despite the significant accuracy demands, the requirements for positioning of the probes are not detrimentally restrictive and can be met in practice. Specifically, a laser alignment survey of the mapper transiting around the ring and a sensitivity analysis determine the impact of the probe position uncertainties on the multipole strengths. This effect generates uncertainties for the azimuthally averaged dipole (12 ppb), normal quadrupole (27 ppb) and skew quadrupole (4 ppb). The azimuthal variations in the magnetic field and muon distributions are incorporated in the muon weighting analysis (< 20 ppb) as well as the beam dynamics simulations described in Sec. II F. The multipole strengths, tracked between field maps by stationary NMR probes outside the storage volume, are highly stable over time; the ranges observed in the Run-1 data set are summarized in Table III. Additional experimental uncertainties from magnetic field tracking (56 ppb) and the presence of fast transients (99 ppb) are carefully quantified resulting in total systematic uncertainties on the determination of the muon-weighted magnetic field of approximately 114 ppb for the Run-1 data set.

F. Beam dynamics simulation tools

Many of the results discussed in this paper incorporate comparison with, or results from, beam dynamics simulations. Several compact simulation packages were used to rapidly estimate effects, but it is the work of three sophisticated and complementary methods that drive the results. To determine critical information, such as momentum-time beam correlations, all three are typically used. In all cases, it is critical that the simulation

	Mean [ppm]	SD [ppm]	Pk-Pk [ppm]
Dipole	1,000,000	1.11	-2.10 – 1.56
Normal quadrupole	0.22	0.34	-0.72 – 0.84
Skew quadrupole	0.75	0.22	0.17 – 1.01
Normal sextupole	-1.38	0.12	-1.56 – -1.14
Skew sextupole	0.57	0.12	0.34 – 0.75
Normal octupole	0.02	0.01	-0.01 – 0.03
Skew octupole	0.31	0.02	0.27 – 0.34

TABLE III. Statistical characterization of the azimuthally averaged multipole strengths (normalized to $r = 45$ mm) relative to the dipole (1.45T) tracked during the Run-1 data set. The mean, standard deviation (SD), and peak-to-peak (Pk-Pk) range correspond to the variations of these azimuthally averaged multipole strengths over time and are significantly smaller than the variation in azimuth. The Pk-Pk of the dipole denote lower and upper deviations relative to its mean.

programs are cross-checked against a set of benchmarks showing that they can evaluate analytically calculated effects with high precision [23]. It is also imperative that they are first tuned to match measurements of the incoming beam properties, the storage distribution within the ring, the CBO amplitudes, frequencies, and their time-dependence, and the stored momentum distribution. We describe their essential features below.

1. GEANT4-based gm2ringsim

The `gm2ringsim` program [24] is a GEANT4 [25] based model of the storage ring and the final focus beamline used to steer the beam into the ring. The model includes all of the active detectors and most of the passive components installed in the storage ring. The geometry is constructed from a mixture of GEANT4 native solids and CADmesh objects [26]. Calorimeters and straw-tracker modules are fully described, as are complex solids, such as the vacuum chambers and their inner structures, and the quadrupole and kicker plates. The geometry for the straw-tracker modules includes coordinates as determined in alignment surveys.

Four sets of realistic time- and space-dependent electric and magnetic fields are implemented. These include a pure dipole magnetic field in the storage region and a radially dependent fringe field that extends toward the center of the ring. Radial magnetic field maps and additional multipole perturbations in the storage region, as described in Section II E, can optionally be included. The inflector magnetic field is implemented as a map. The time-dependence of the kicker magnetic field is taken from direct magnetometer measurements made at the center of the plates (see Fig. 1). The spatial field map within the kicker region is obtained using the finite-element magnetics modeling package OPERA [27]. The strength and timing of the kicker with respect to the injected beam can be adjusted independently for each of

the three kicker plates. The fields associated with the electrostatic quadrupole plates are implemented as a multipole expansion. They are dynamically evolved through the scraping periods at the beginning of each muon fill, and they can accommodate the perturbations and independent time constants caused by the damaged resistors during Run-1.

Simulated data sets are typically generated using two types of “particle guns.” The *beam gun* imports muon distributions at the end of the final focus beamline as determined from `G4Beamline` simulations of the Muon Campus beam and injects them into the storage ring. The beam gun allows for the injection of a mixture of particles, facilitating studies of proton and positron contamination. The *gas gun* omits the injection process completely and instead fills the storage region phase space of the ring with muons that then decay at that location. This distribution of muons is matched to reflect the measured vertical and radial offsets of the beam within the storage ring as well as the measured coherent betatron oscillation amplitudes. The gas gun is particularly useful for positron acceptance and reconstruction studies. In both cases, muon spin is appropriately evolved during time-in-fill, and proper spin-dependent muon decays are employed.

2. COSY INFINITY

The COSY-based model [28] is a data-driven computational representation of the storage ring. Dedicated packages in `COSY INFINITY` [29] for the design and analysis of particle optical systems provide the framework for beam physics studies and symplectic tracking simulations in the storage ring. The beam dynamics of the injected muon beam is recreated with high fidelity by representing the magnetic and electric guide fields in the storage region based on measurements of the beam.

The magnetic field inhomogeneities of the storage ring are determined from the magnitude of the magnetic field as measured by the NMR probes (see Sec. II E). Due to the high uniformity of the magnetic field along the vertical direction in the storage region, a reliable extraction of magnetic multipole strengths from the experimental data is performed and implemented in the model as a series of magnetic multipole lattice elements. Each ESQ station is modeled as an optical element superimposed on the magnetic field. The nonlinear action of the ESQ on the beam’s motion is captured by accounting for the high-order coefficients of the electrostatic potential’s transverse Taylor expansion. These coefficients are calculated by recursively iterating the horizontal mid-plane coefficients – modeled with conformal mapping methods [30] – to satisfy Laplace’s equation in curvilinear optical coordinates. The effective field boundary and fringe fields of the ESQ are calculated [30] using `COULOMB`’s [31] boundary element method field solver.

With the aforementioned electric and magnetic guide

fields implemented in the COSY-based model, the orbital and spin equations of motion are well defined and integrated to produce high-order transfer maps via differential algebra methods [32]. Transfer maps are computed and combined to recreate either azimuthal segments or the entire storage ring.

Beam tracking simulations are performed by preparing transfer maps of the storage ring. The muon beam, represented as an array of orbital and spin coordinates around the closed orbit, is transformed turn-by-turn with transfer maps that encapsulate the time-evolving guide fields as they vary throughout the beam fill. Symplecticity is enforced during beam tracking with high-order transfer maps to account for the truncation of components beyond the map order, in this way controlling energy conservation and error propagation. To account for beam collimation, special routines were developed to efficiently remove muons beyond the collimator apertures and only at the azimuthal locations where they are inserted. This tool, together with the symplectic enforcement during tracking, allows for reliably studying muon loss rates in the storage ring.

The beam conditions after the action of the injection kickers are obtained by preparing high-order transfer maps of the azimuthal segments where the three kickers are placed. Using these maps combined with the transfer maps of the other components of the storage ring, a beam distribution obtained from simulations of the Muon Campus beamlines and the inflector is transferred into the ring’s storage region. The structure and time-dependent strength of the kicker magnetic fields are constructed from magnetometer measurements (see Fig. 1). Alternatively, the initial beam distribution after injection is also prepared by calculating with a nonnegative least-squares solver the probability density functions of the beam, based on data from the straw tracking detectors and the fast-rotation analysis (see Sec. III).

The COSY-based model has been extensively used to calculate lattice configurations (e.g. periodic Twiss parameters, betatron tunes, closed orbits, and dispersion functions) of the storage ring with and without the damaged ESQ resistors. It provided a reconstruction of the special electric field behavior of the ESQ electric fields during Run-1 for the assessment of beam dynamics systematic uncertainties. Further, it has provided a numerical model to link tracker measurements with direct HV probe measurements of the damaged ESQ resistors, and it has been used to choose optimal configurations of the storage ring to minimize muon losses.

3. BMAD

BMAD refers to a subroutine library [33] for simulating the dynamics of relativistic beams of charged particles, and an associated format for defining beam line elements. So defined, the full complement of the analysis tools of the library can be used to investigate the particle dynam-

ics. Particle tracking methods include Taylor maps, symplectic integration, and Runge Kutta integration through field maps. Taylor maps can be predefined or constructed by tracking.

The BMAD formatted representation of the $g-2$ experiment is comprised of three distinct branches: 1) the M5 beam line; 2) the injection channel and inflector; and 3) the storage ring, including a static magnetic field, time-dependent quadrupole electric fields and kicker magnetic fields, and collimator apertures. The beam lines are assembled as a sequence of elements with fixed length. The electromagnetic fields in each element are defined by field maps, multipole expansions, or analytic expressions. Time-dependence for pulsed kickers and ramped quadrupoles requires custom code. Specialized custom routines are used to incorporate arbitrary kicker pulse shapes or quadrupole voltage time-dependence. The curvilinear coordinate system can be represented by beginning with a full 3-dimensional map, and then extracting an azimuthal slice of the map (in x, y at fixed ϕ) or with a fitted multipole expansion of McMillan functions. The curvature necessarily introduces nonlinearities that are not faithfully included in a 2-dimensional Cartesian expansion. The BMAD code allows specification of the quadrupole electric field in terms of field maps or multipoles. The main magnet is represented as a map or analytic function with uniform field. A uniform radial component can be specified. Measured field errors are incorporated analytically. The azimuthal dependence of the error field is expanded as a solution to Laplace's equation in cylindrical coordinates in order to ensure consistency with Maxwell equations. The magnetic field through the hole in the back-leg iron and cryostat and main magnet fringe field is based on a 3-dimensional OPERA [27] map. A distinct map is computed for the field in the inflector. The fringe and inflector maps are superimposed as appropriate.

III. DETERMINATION OF THE STORED MUON MOMENTUM DISTRIBUTION

The contribution to ω_a^m from the electric field depends on the momentum distribution of the stored muon beam, or equivalently the equilibrium radial distribution. Since the azimuthal speed of the stored muons is nearly uniform over the 9 cm aperture, to a good approximation a muon's rotation frequency is inversely proportional to its equilibrium radius x_e . Because the muons are stored over a range of x_e , a beam bunched at $t = 0$ will steadily debunch, as the higher frequency muons at smaller radii advance with respect to the lower frequency muons at larger radii.

A technique [34] based on Fourier transformation yields a frequency spectrum that can be converted to radius and momentum. An alternative method extracts the radial distribution by a direct fit to the debunching signal of the muon beam [1, 35]. In both cases, the

input data are provided by the calorimeters, which measure the time-dependence of the intensity of the decay positron distribution. The positron counts from the 24 calorimeters are merged together with a time offset of $T/24$ per calorimeter where T is the cyclotron period, approximately 149 ns. The upper panel of Fig. 4 shows the intensity 4–5 μs after injection; the lower panel expands the time range to 4–14 μs . The individual turns around the ring, referred to as “fast rotation”, are distinct. The slower modulations in the upper envelope are caused by muon decay and the ω_a^m precession frequency. By the nominal precession fit start time of 30 μs , the rapid cyclotron frequency modulation has largely dephased and eventually disappears. To isolate this fast rotation signal, the calorimeter time spectra are divided by a fit⁵ to the envelope modulation using Eq. 4, which effectively removes all the significant physics signals *except* the fast rotation itself.

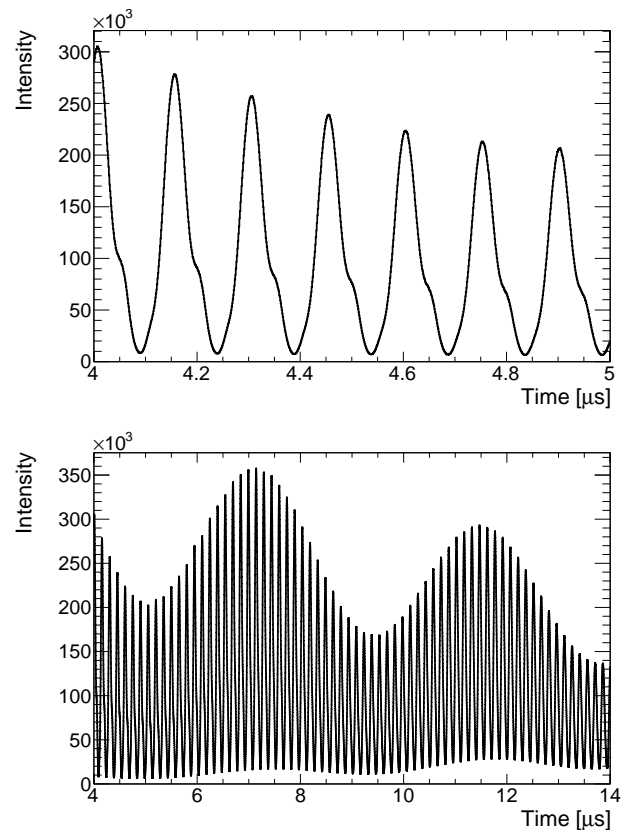


FIG. 4. Positron counts as a function of time as seen by all the calorimeters combined for the Run-1d data set for the time ranges: (top) 4–5 μs and (bottom) 4–14 μs with respect to the beam injection. The time binning period is 1 ns. The amplitude modulation in the bottom panel is from the muon spin rotation frequency ω_a^m .

⁵ In the full fits of the precession data, the function has additional terms, but the simple form of Eq. 4 is perfectly sufficient for this Fourier analysis.

A. Momentum-Time Correlation

The Fourier and debunching methods, discussed below in Sections III B and III C, both assume that the momentum distribution in the captured muon pulse is uncorrelated with the longitudinal position in the pulse train (see Fig. 1). If the momentum and time are uncorrelated, the distribution is maximally bunched when it enters the ring. The peak intensity of the fast rotation signal only decreases with time. The behavior is symmetric with respect to time reversal. One can imagine that the peak intensity likewise decreases moving backwards in time.

In reality, a momentum-time correlation is introduced by the injection kicker. The efficiency with which muons are captured in the ring depends on momentum and the amplitude of the kicker. If the kicker field is low, acceptance is higher for high-momentum muons; if the kicker field is high, low-momentum muons are favored. Since the magnetic field of the kicker varies over the time duration of the incoming muon pulse, so do the momenta of muons that are stored in the ring. Simulations are used to characterize the momentum-time correlation of the captured muons, and to estimate the systematic uncertainty in the measurement of the momentum distribution from the fast rotation analysis.

B. Frequency domain fast rotation analysis: Fourier method

For a stored muon beam in which the cyclotron frequencies and injection times are independent, the frequency distribution of the ensemble can be extracted by the cosine transform of the fast rotation signal $S(t)$, [34]

$$\hat{S}(\omega) = 2 \int_0^{\infty} S(t + t_0) \cos(\omega t) dt, \quad (9)$$

where t_0 is an effective time of symmetry for the ensemble. The optimal t_0 is determined by imposing that the transform $\hat{S}(\omega)$ must vanish in the unphysical frequency region outside the range that can be stored.

The problem is complicated by the fact that the first few microseconds of the fast rotation signal are contaminated by beam positrons and by muons that will not be stored. The analysis is based on the intensity signal that begins at about 25 turns, or $t_s = 4.1 \mu\text{s}$ after injection, by which time the beam positrons have been lost and the performance of the calorimeter SiPMs has largely recovered from the intense flash of particles at injection. The available cosine transform is therefore missing the contribution before the start time t_s , which introduces a background modulation $B(\omega)$ to the frequency spectrum. As shown in [34], this background can be estimated using an inverse cosine transform and a model for the frequency

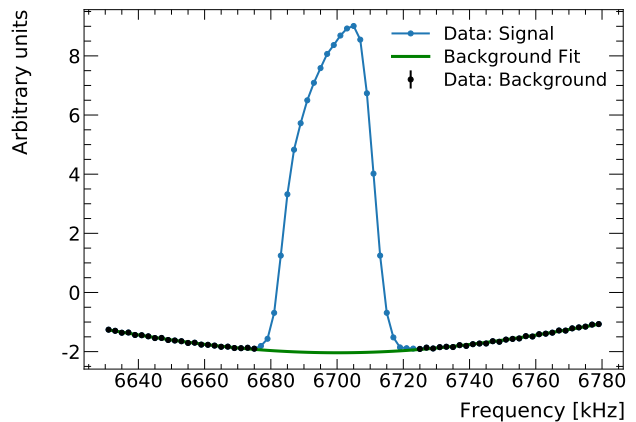


FIG. 5. The frequency distribution obtained with a cosine transform of the fast rotation signal from the Run-1d data set. The background is a consequence of the missing data before the start time of $4 \mu\text{s}$. A cardinal sine (sinc) background fit has been applied to the black points and is subtracted from the whole frequency range as a correction.

distribution \hat{S}_0 with the result

$$B(\omega) \approx \frac{1}{\pi} \int_{\omega_-}^{\omega_+} \hat{S}_0(\omega') \frac{\sin[(\omega' - \omega)(t_s - t_0)]}{(\omega' - \omega)} d\omega', \quad (10)$$

where the limits of integration correspond to the physical range of frequencies that can be stored. An ansatz for $\hat{S}_0(\omega)$ is hypothesized and the parameters determined by a fit to the background. If $\hat{S}_0(\omega) = A\delta(\omega - \omega_B)$, where A and ω_B are fit parameters for amplitude and frequency respectively, then

$$B(\omega) \approx \frac{A \sin[(\omega_B - \omega)(t_s - t_0)]}{\pi (\omega_B - \omega)}. \quad (11)$$

Empirically, this model is found to give a good fit to the background for start times before $5 \mu\text{s}$. More sophisticated functional forms give good background fits for start times up to $t_s \sim 25 \mu\text{s}$ in Monte Carlo simulation, and in practice, the fitted spectrum is nearly independent of start time for $4 \mu\text{s} < t_s < 25 \mu\text{s}$. An example of the frequency transform \hat{S} of Eq. 9 is shown in Fig. 5, with an optimal background fit using Eq. 11. The background fit is subtracted, and the corrected transform is taken as the distribution of cyclotron frequencies.

C. Time domain fast rotation analysis: debunching method

An alternative approach, pioneered by the CERN II collaboration, is based on a simple model of the beam's debunching at early times in the measurement period [1, 35]. Consider first the contribution to the fast rotation signal from a narrow bin in time and momentum space. The signal is initially rectangular, but grows

increasingly trapezoidal as it revolves around the ring, due to the uniform momentum spread within the bin. Mathematically, all the essential physics is captured in the propagator function β_{ijk} , which describes this segment's contribution to the overall signal in the detector at time t_j . Indices i and k identify the segment's equilibrium radius and position in time within the injected muon bunch, respectively. Using superposition, an ensemble of segments with joint distribution $f_i I_k$ is given by

$$S_j = \sum_{ik} \beta_{ijk} f_i I_k. \quad (12)$$

Here S_j is the calorimeter signal in time bin j , f_i describes the radial distribution, and I_k describes the time profile of the injected beam. A least squares fit to the signal S_j determines f_i and I_k .

In the BNL experiment [3], many of the calorimeters were live on the first turn following injection. It was therefore simple to make a very good guess of the stored beam's initial time profile, I_k . As noted above in Sec. III B, detector signals in the Fermilab experiment cannot be used before 4 μ s after injection. Therefore, the original CERN method was replaced with a pair of fits, for f_i and I_k , which are iterated until the results are stable. In the first pair of fits, the time profile is taken from the calorimeter signal at 4 μ s and the momentum distribution is determined by the fit. Then that momentum distribution is used to update the injected time profile in a second fit. The determination of the momentum and time distributions are computationally identical. Between 50 and 100 iterations of this double fit are generally required for convergence.

D. The radial distributions for Run-1

An example of the radial distribution extracted by both the Fourier method and the debunching analysis is shown in the top panel of Fig. 6. The agreement is sufficiently good that either can be used to extract the electric field correction. The radial distributions for the Run-1a, 1b, 1c, and 1d periods as determined by the Fourier method are shown in the bottom panel of Fig. 6. The slightly different distributions are attributed primarily to the different kicker strengths, as indicated in Table I. The means of the radial distributions – in all cases – do not fall on the magic radius. This fact will enter in the calculation of the electric field correction in Section IV. The radial offsets and widths as determined by the Fourier method are given in Table IV.

IV. ELECTRIC FIELD CORRECTION, C_e

The electric field term in Eq. 5 produces a rest frame magnetic field that affects the measured anomalous pre-

Data Set	x_e (mm)	σ (mm)
Run-1a	6.1 ± 1.2	9.2 ± 0.2
Run-1b	4.9 ± 1.2	9.2 ± 0.2
Run-1c	6.3 ± 1.2	9.2 ± 0.2
Run-1d	6.7 ± 1.2	8.9 ± 0.2

TABLE IV. The radial offsets, x_e , and widths, σ , for the four Run-1 data sets obtained by the Fourier method.

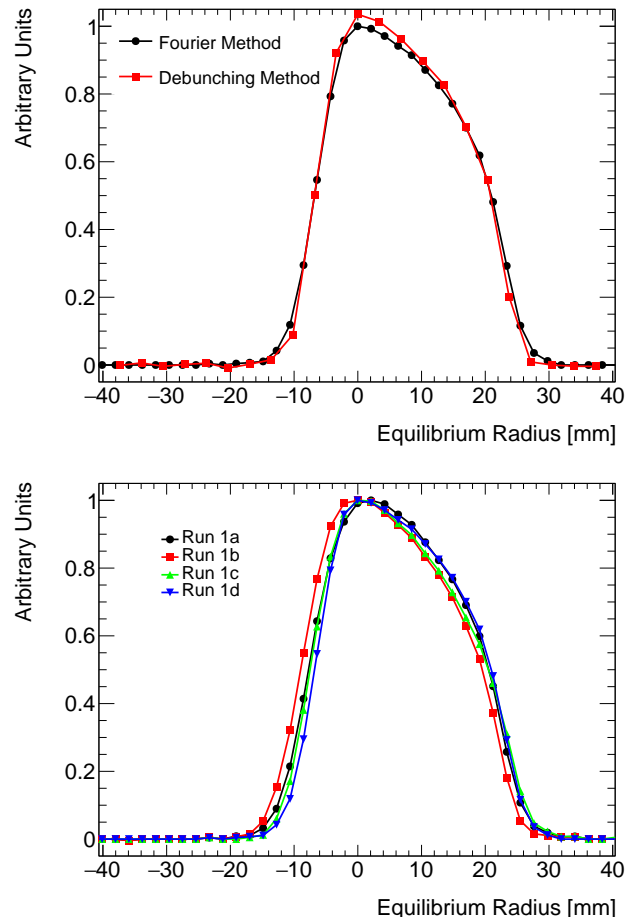


FIG. 6. Top: The radial (closed orbit) distribution extracted by both the Fourier method and the debunching analysis for the Run-1d data set. Bottom: The radial distribution for the four Run-1 data sets as determined by the Fourier method. In both plots, the equilibrium radius is defined such that a magic momentum muon is at 0 mm.

cession frequency ω_a^m . For the simple case where we neglect the vertical betatron motion and $\vec{\omega}_a = \vec{\omega}_s - \vec{\omega}_c$, Eq. 5 can be simplified to

$$\omega_a^m = \frac{|q|}{m} a_\mu B_y \left[1 - \beta \frac{E_r}{c B_y} \left(1 - \frac{m^2 c^2}{a_\mu p^2} \right) \right] \quad (13)$$

where ω_a^m is a scalar frequency and the subscripts r and y denote the radial and vertical components respectively. The electric field term vanishes at the magic momentum

$p_0 = (mc)/\sqrt{a_\mu}$, or when $E_r = 0$ which is the case at R_0 as a result of the design of the ESQ system. In practice, the stored muon distribution has a finite momentum spread and is not centered, as discussed in Sec. III and shown in Fig. 6. The mean radial electric field experienced by a muon oscillating about an equilibrium radius x_e in an ideal electric quadrupole is

$$\langle E_r \rangle = \kappa x_e = \frac{n\beta c B_y}{R_0} x_e, \quad (14)$$

where κ is the electric field gradient. Defining $p = (p_0 + \Delta p)$ and using

$$\frac{\Delta p}{p_0} = (1 - n) \frac{x_e}{R_0}, \quad (15)$$

where the approximation that the dispersion is a constant value of $R_0/(1 - n)$ is sufficient, we average over the entire muon distribution to obtain the electric field correction

$$C_e \approx 2n(1 - n)\beta_0^2 \frac{\langle x_e^2 \rangle}{R_0^2}, \quad (16)$$

where $\beta_0^2 = p_0^2/[m^2c^2 + p_0^2]$. The correction must be applied to the measured ω_a^m to obtain the anomalous precession frequency ω_a used to determine a_μ . The use of an analytic expression for the electric field correction has been previously considered [19, 36, 37]. The precision goals of our experiment require careful consideration of this correction. An extensive discussion of electric quadrupole nonlinearity factors is given in Appendix A and numerical tests to justify the validity of the use of Eq. 16 are given in Appendix B.

A. Measuring the muon radial distribution and calculating C_e

The fast rotation analysis using the Fourier method (see Sec. III B) yields the distribution of cyclotron frequencies f , which are converted to equilibrium radii R by the relation $R(2\pi f) = v$, assuming fixed muon velocity v . The radial offsets x_e relative to the magic radius $R_0 = 7112$ mm are therefore $x_e = v/(2\pi f) - R_0$. This conversion yields the distribution of equilibrium radial offsets, as in Fig. 6. The electric field correction depends on the mean and width of this distribution, via $\langle x_e^2 \rangle = \sigma_{x_e}^2 + \langle x_e \rangle^2$.

The recovered radial mean and width exhibit some variation when the fast rotation analysis is repeated over a range of positron energy bins. This is a consequence of variations in calorimeter acceptance with positron energy and radial decay position, supported by simulation with `gm2ringsim`. The final C_e is therefore weighted over positron energy bins according to the statistical power of ω_a^m in each bin. For an asymmetry-weighted analysis⁶, this is the average of C_e over positron energy bins

between 1 GeV and 3.1 GeV, weighted by $N(E)A(E)^2$, where $N(E)$ is the number of positron counts in energy bin E and $A(E)$ is the fitted asymmetry of the ω_a^m modulation in that bin. The resulting corrections C_e are tabulated with their dominant uncertainties in Table V, as discussed below.

The statistical uncertainties in $\langle x_e \rangle$, σ_{x_e} , and C_e are estimated by repeating the fast rotation analysis over an ensemble of pseudo-data. Each positron count N_i in the measured time spectrum is shifted by $\pm\sqrt{N_i}$ at random, assuming uncorrelated Poisson statistics. The analysis is repeated over about 1000 randomly altered signals, and the ensemble standard deviation of each recovered quantity is taken as its statistical uncertainty. For subsets of the data with different total positron counts N , the statistical uncertainty was confirmed to scale as \sqrt{N} .

The fast rotation Fourier analysis method relies on several chosen parameters, including the start and end times of the cosine transform, the frequency bin spacing, the frequency distribution model used in the background fit, and the set of frequency bins included in that fit. In each case, a scan is performed over the range of appropriate choices, and the standard deviation in the result is taken as the corresponding systematic uncertainty. The total uncertainty attributed to these parameters is the average of their linear sum and quadrature sum, accounting for probable correlations.

Furthermore, Eq. 9 does not extract the frequency distribution perfectly as intended when there is any systematic relationship between cyclotron frequency and injection time. Referred to here as momentum-time correlation, this relationship is expected as discussed in Section III A. The corresponding uncertainty in C_e has been estimated as 52 ppb, which is the average discrepancy between truth and reconstruction using `gm2ringsim` and `BMAD` simulations.

The expression for C_e in Eq. 16 is derived under the assumption of continuous ESQ plates and ideal alignment of the quadrupole field relative to the target muon orbit. The effects of discrete ESQ plates, position misalignments, and voltage errors have been studied using `BMAD` simulations with surveyed ESQ positions and their measurement uncertainties. The resulting uncertainty in C_e is estimated to be about 6.4 ppb.

The field index n has been measured using the value of ω_{CBO} fitted during the production of the fast rotation signal, and the relationship $\omega_{\text{CBO}} = \omega_c - \omega_x = (1 - \sqrt{1 - n})\omega_c$ from Sec. II A. However, the CBO frequency is not constant throughout the fill, rather approaching a stable value with two exponential time constants based on the beam scraping procedure and damaged ESQ resistors. This time-dependence has been measured using the tracking detectors (see Sec. VI A), and

⁶ The positron spectrum constructed by weighting each e^+ con-

tribution to the time series by its energy-dependent asymmetry, shown to be the optimal approach [38].

Data Set	Run-1a	Run-1b	Run-1c	Run-1d
C_e	471	464	534	475
Stat. uncertainty	< 1	1	< 1	< 1
Fourier method	8	13	14	4
Momentum-time	52	52	52	52
ESQ calibration	6	6	6	6
Field index	2	2	2	4
Syst. uncertainty	53	54	54	53

TABLE V. Electric field corrections C_e (ppb) and uncertainties combined in quadrature (ppb) for the four Run-1 groups.

the uncertainty in n has been estimated using the RMS spread in ω_{CBO} over the ω_a^m measurement period.

V. PITCH CORRECTION, C_p

The ESQ system used to vertically confine the muon beam creates vertical betatron oscillations; that is, periodic up - down pitching of the vector $\vec{\beta}$. The $a_\mu \vec{\beta} \times \vec{B}$ term in Eq. 5 affects the value of ω_a^m . The magnitude of the term is reduced when $\vec{\beta}$ and \vec{B} are not perpendicular as is the case here. The vertical betatron frequencies ω_y listed in Table II are an order of magnitude larger than the muon spin rotation frequency ω_a , which avoids depolarizing spin resonances. These topics were first recognized and discussed in [39, 40] where the pitch correction C_p is derived as

$$C_p = \frac{n \langle y^2 \rangle}{2 R_0^2} = \frac{n \langle A^2 \rangle}{4 R_0^2}. \quad (17)$$

The vertical oscillation amplitude A can be extracted from measurements by the tracker detector system. The validity of Eq. 17 has subsequently been confirmed and explored further [23, 41, 42]. Appendix B describes our numerical simulations that also reaffirm Eq. 17 and furthermore permit modeling of the uncertainty on C_p owing to the use of flat electrodes, ESQ plate misalignment, and voltage errors.

A. Measuring the muon vertical distribution and calculating C_p

The vertical distribution of decay positrons is measured by the straw trackers, as shown for a subset of the data in Fig. 7a. Throughout Run-1, the temperature in the experimental hall slowly increased from 24.5° C to 28.5° C, and exhibited typical diurnal fluctuations of roughly 1° C. These changes produced a slowly varying radial component to the magnetic field, which caused the vertical mean of the beam to change with time. To account for this effect, these data were subdivided into shorter running periods, and a weighted average of their corresponding pitch corrections was computed. When

determining the vertical muon distribution, time cuts are applied, which restricted the tracker data to the same time interval used for the measurement of the anomalous spin precession frequency.

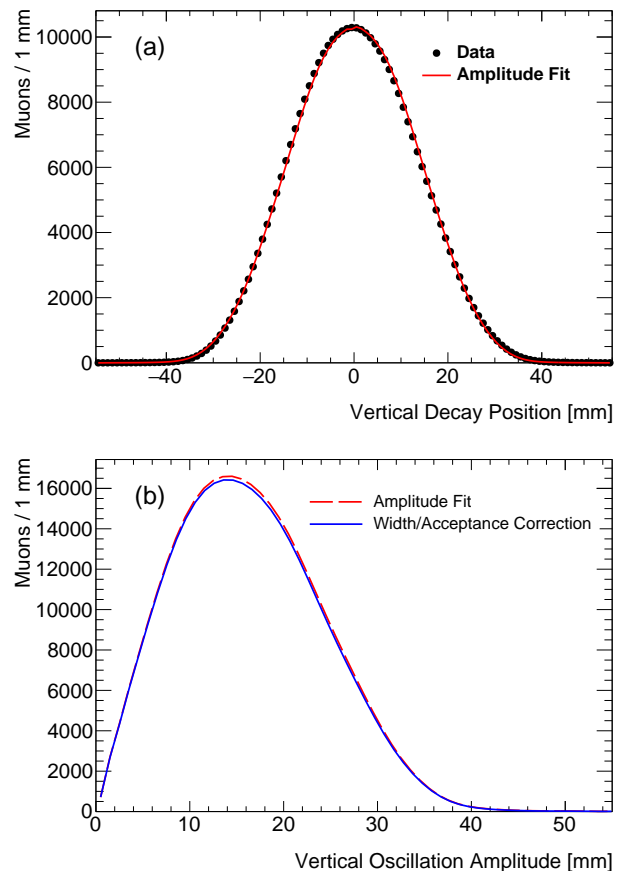


FIG. 7. (a) The vertical distribution of muons from a subset of Run-1a after applying tracker resolution and acceptance corrections. (b) The fitted distribution of vertical oscillation amplitudes, before (dashed red) and after (solid blue) the azimuthal averaging and calorimeter acceptance corrections described in the text.

The tracker measurements yield a good estimate of the true vertical distribution of the muon beam at the location of the tracker stations. However, it is necessary to take into account azimuthal variations around the storage ring from the discrete ESQ sections. The effective vertical distribution seen by the calorimeters that measure ω_a^m must also be determined.

In order to address azimuthal variations in the vertical distribution of the muon beam, the vertical beta functions β_y are evaluated as a function of azimuthal coordinate ϕ using `gm2ringsim` and `COSY`. By taking the ratio of $\sqrt{\beta_y(\phi)}$ with the value at each tracker station, the scale factor which relates the vertical width at each tracker station to any other azimuthal coordinate is obtained. The vertical distribution from a single tracker station is then averaged over azimuth by stretching or

shrinking the width ratio in each azimuthal slice using $\sqrt{\beta_y(\phi)}$.

Not all decay positrons hit a calorimeter and enter into the determination of ω_a^m . To account for this, each calorimeter's acceptance has been estimated as a function of transverse and azimuthal decay position using `gm2ringsim` (see Fig. 28). In each azimuthal slice of the storage ring, the transverse acceptance function is integrated over the radial dimension to produce an effective vertical acceptance function. Then, during the azimuthal averaging procedure, the vertical distribution in each azimuthal slice is masked by the corresponding calorimeter acceptance function after stretching by the vertical width ratio. The nominal results use the acceptance functions for all calorimeters combined, treating the acceptance per-calorimeter as a cross-check. Furthermore, the calorimeter acceptance functions are subdivided by positron energy bin. Therefore, the pitch correction is evaluated using calorimeter acceptance from each positron energy bin, and the results are averaged according to the statistical power of ω_a^m in each energy bin.

When considering calorimeter acceptance, the pitch correction can no longer be evaluated using $\langle y^2 \rangle$ as in Eq. 17. This is because the simple relation between the pitch angle and $\langle y^2 \rangle$ along an oscillation breaks down when the vertical positions are not evenly weighted. Instead, the right-hand side of Eq. 17 is used with $\langle A^2 \rangle$ from the distribution of oscillation amplitudes, which accurately describes the distribution of measured pitch angles when vertical acceptance is present. The amplitude distribution may be recovered from the trackers' vertical decay distribution by defining the fit function

$$\langle N_j^y \rangle = \sum_i N_i^A P(y_j | A_i), \quad (18)$$

where $\langle N_j^y \rangle$ is the expected number of decays in the j^{th} position bin, N_i^A is a fit parameter for the number of muons in the i^{th} amplitude bin, and $P(y_j | A_i)$ is the calculable constant probability that a muon from the i^{th} amplitude bin decays to the j^{th} position bin. The amplitude distribution is extracted from a fit to tracker measurements of the vertical counts in each bin, N_j^y , after correcting for the intrinsic tracker acceptance and resolution. The fit result and corresponding amplitude distribution are shown in Fig. 7a and Fig. 7b respectively. The amplitude distribution is stretched and averaged over azimuth as described above, and each amplitude bin A_i is weighted by the average of the calorimeter acceptance over all position bins y_j using $P(y_j | A_i)$. The result of these corrections is shown by the solid blue line in Fig. 7b. Finally, the pitch correction is calculated using Eq. 17 with $\langle A^2 \rangle$.

Since the corrections have a small effect, the statistical uncertainty of C_p can be estimated using the statistical uncertainty of the measured vertical width σ_y , propagated to $C_p \propto \sigma_y^2$. The dominant systematic uncertainty is from the straw tracker alignment and reconstruction.

There are smaller contributions from the acceptance and resolution corrections. Other possible sources of uncertainty come from the estimation procedure for C_p described above, as well as possible errors in alignment and calibration of the ESQ system that are described in detail in Appendix B.

Data Set	Run-1a	Run-1b	Run-1c	Run-1d
C_p (ppb)	176	199	191	166
Stat. uncertainty	< 1	< 1	< 1	< 1
Tracker reco.	11	12	12	11
Tracker res. & acc	3	4	4	3
$\beta_y(\phi)$ & calo. acc.	1	1	2	1
Amplitude fit	1	< 1	1	3
ESQ calibration	4	4	4	4
Syst. uncertainty	12	14	14	12

TABLE VI. Pitch corrections C_p (ppb) and uncertainties (ppb) for each run group in Run-1. The total systematic uncertainty is the quadrature sum of the individual contributions.

The resulting values for C_p are summarized in Table VI. The corrections vary from 166 to 199 ppb with the main driver behind the range being the different ESQ settings for the different data sets. Differences with the same n -value arise due to different radial magnetic fields. The statistical uncertainty is negligible and the systematic uncertainty is well under control at the 12 to 14 ppb level.

VI. DYNAMIC EFFECTS OWING TO TIME-CHANGING FIELDS

A. Changes to the betatron frequencies

The slower voltage increase on the Q1L upper and lower ESQ plates as a result of the damaged resistors in Run-1 introduces time-dependencies of the storage ring lattice parameters (see the dotted blue and solid orange traces in Fig. 3). Electric normal quadrupole and skew dipole terms are largely proportional to the sum and difference in high voltage between the top and bottom electrodes, respectively, making the beta functions, radial dispersion function, and the closed orbits time-dependent during the measurement period. Figure 8 illustrates the difference in the electrostatic potential in the Q1L ESQ section versus time-in-fill with respect to the nominal case for all other ESQ sections, which had normal resistors and stable voltages by 30 μs . The beta functions are a consequence of the focusing gradient configuration in the ring, which depends on the normal quadrupole terms at each ESQ section. The solid black line in Fig. 8 illustrates the added quadrupole field at Q1L that introduces a time-dependence to the beta functions. The vertical closed orbit is distorted by skew dipole terms from the guide fields, the time-dependence of which corresponds

to the value of the dashed blue line in Fig. 8.

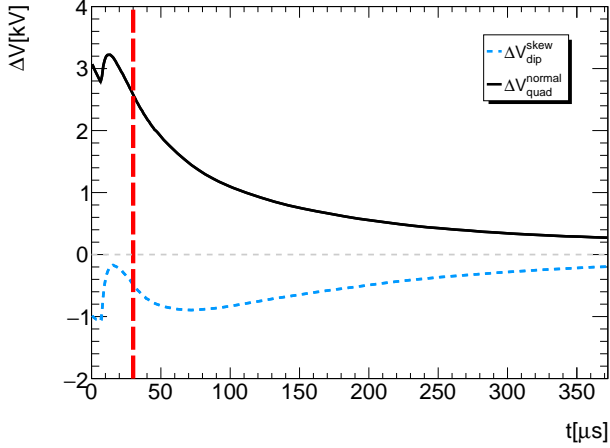


FIG. 8. Additional electrostatic potential at $r = 5$ cm versus time for the ESQ powered through damaged resistors. The skew dipole (dashed blue) and normal quadrupole (solid black) terms are shown relative to the nominal case and correspond to a 2D Taylor expansion based on data collected after Run-1 using an HV probe. The vertical dashed red line at $30 \mu\text{s}$ after injection indicates the nominal start of the precession fits. Scraping ends at $7 \mu\text{s}$ after injection, visible at the abrupt kinks in the curves. Nominal ESQ plates rise with a nominal RC time constant of $\tau \approx 5 \mu\text{s}$, but these ESQ plates show prolonged and asymmetric time constants which lead to focusing and vertical steering errors during the data taking period.

Figure 9 shows the calculated beta functions β_y and β_x , and the dispersive function D_x for Run-1a early and late in the fill; the latter is well after the ESQ voltages are at their intended values. The vertical shaded regions in this figure correspond to the locations in azimuth of the short and long ESQ sections, with Q1S at $\phi = 30^\circ$. The dynamic functions match the time-dependence of ω_{CBO} and the vertical width (VW) frequency associated with the vertical breathing of the muon beam, and the slow changes of vertical beam mean y and width $\sqrt{\langle y^2 \rangle}$.

The tracker detectors are capable of reconstructing the stored muon distribution at different times within the fill and are therefore used to measure the betatron oscillation parameters as well as any slow drift of the beam position or width. The betatron frequencies can be determined to high precision: in fact, it was analysis of tracker data that first drew attention to a possible time-dependence of the electric quadrupole field. The measured betatron frequencies are necessary to verify the tune, and the measured betatron amplitudes are used in the optimization of kick strength and inflector deflection angle.

After the end of scraping, with stable voltages during the measuring period, ω_{CBO} and ω_{VW} should not change. However, in Run-1, they continued to evolve after $30 \mu\text{s}$ by 1.5% in Run-1a, 1b and 1c, and by 3.0% in Run-1d.

Figure 10 shows tracker measurements of ω_{CBO} for

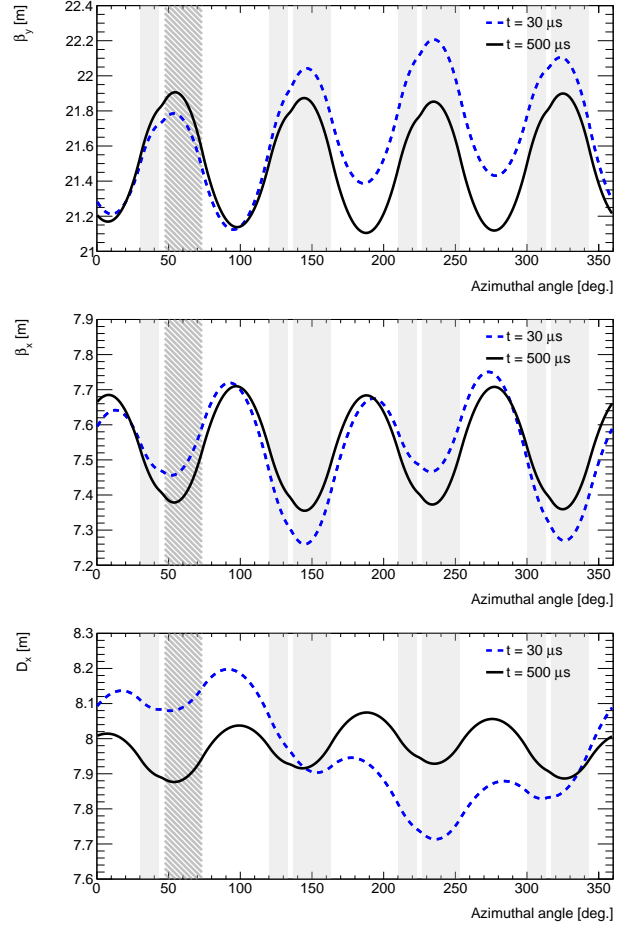


FIG. 9. The calculated β_y (top), β_x (middle), and dispersion D_x (bottom) functions versus azimuth in the ring at times $30 \mu\text{s}$ and $500 \mu\text{s}$ after injection for the Run-1a data set. The calculation includes the effect of the damaged resistors used in the Q1L ESQ section (hatched region) and the measured magnetic field distortions versus azimuth. The vertical shaded regions correspond to the locations in azimuth of the short and long ESQ sections.

Run-1a and Run-1d. The fit function contains two exponential terms that describe $\omega_{\text{CBO}}(t)$ well. The first of these is a fast ($\sim 7 \mu\text{s}$) term, which relates to the changing field during scraping. The second term has a longer time constant of $\sim 60 \mu\text{s}$ in Run-1a, 1b and 1c, and $\sim 80 \mu\text{s}$ in Run-1d. This term arises from the damaged resistors and the change in their average value during Run-1d due to their further deterioration.

The fits to the precession data require an accurate model of $\omega_{\text{CBO}}(t)$ to obtain a good χ^2 and stable fit results when changing the fit start time. We note that the correlation between ω_a^m and ω_{CBO} in the fit is small ($\sim 2.4\%$). Varying the time-dependence of the CBO frequency within allowable bands determined from the tracker measurements yields a less than 10 ppb shift to the fitted ω_a^m frequency. The effect from the VW is even

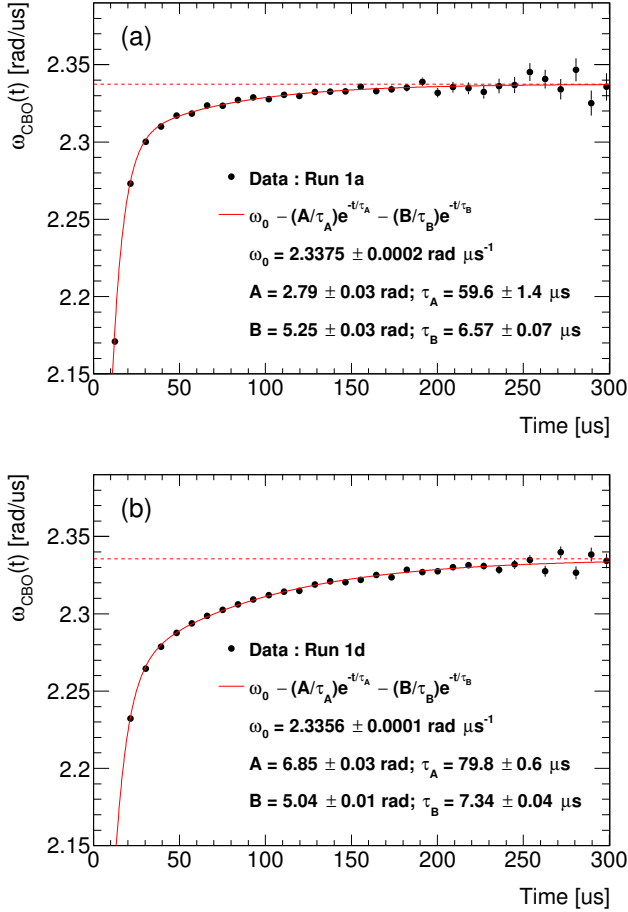


FIG. 10. Tracker measurements of ω_{CBO} in different time slices during the muon fill from the 270° tracker station. (a) and (b) show the Run-1a and Run-1d data sets, respectively. The fit function and parameters are noted in the figure, together with their uncertainties. The difference between the two data sets is attributed to worsening performance of the damaged ESQ resistors. The time-dependence of the frequency is included in the fits of the positron data from the calorimeters to accurately incorporate the CBO acceptance dependence.

smaller than that from the CBO, and it has a negligible effect on the precession fits.

B. Changes to the muon spatial distribution

Because the damaged resistors were connected to the same Q1L plates, and because the circuitry at station Q1L had RC characteristics that differed from the nominal charging conditions (see Fig. 3), we observe a physical effect on the mean and width of the muon distribution. The asymmetrical charging of the top and bottom plates in Q1L created an unbalanced quadrupole component of the ESQ field. This led to a time-dependent focusing gradient, resulting in sub-mm drifts in the beam widths and

radial closed orbit distortions from the time-dependent optical lattice. The vertical closed orbit also manifested an in-fill temporal evolution owing to an introduced skew dipole field at Q1L. Figure 11 displays the time-varying vertical mean and RMS measured by the 180° tracker for the Run-1d data set, which is by far the worst case. In the range $30 - 300 \mu\text{s}$, the vertical mean shifts by approximately 0.5 mm . Note, the absolute vertical scale is not known to better than $\sim 1 \text{ mm}$ owing to alignment uncertainty and the local radial magnetic field. The vertical RMS versus time-in-fill is unstable at the nominal fit start time of $30 \mu\text{s}$, but by $50 \mu\text{s}$ has flattened out, which is when the measurement period for this data set starts. As noted previously, β_y , which is proportional to $\langle y^2 \rangle$, varies around the ring, so one does not expect the magnitude of the width change to be constant versus azimuth.

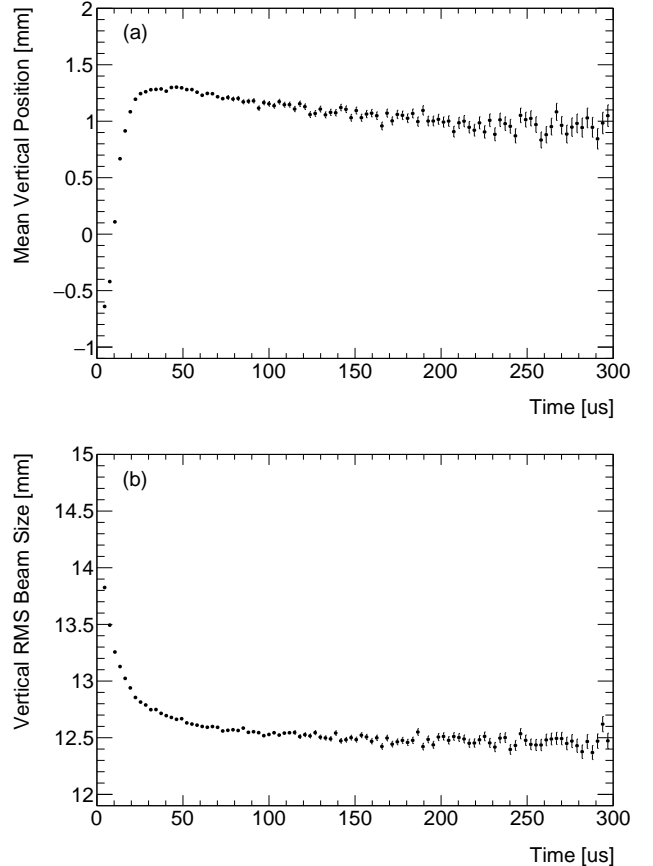


FIG. 11. The 180° tracker station determination of the vertical mean (a) and width (b) versus time-in-fill for Run-1d. The rapid oscillations owing to vertical and horizontal betatron motion have been randomized out to reveal the underlying time-dependence of the mean and width (see also Sec. VIII A).

The tracker station measurements are limited to the 180° and 270° locations in the storage ring. However, the 24 calorimeter stations are positioned at regular in-

tervals covering the complete azimuth. The segmented calorimeters provide a measure of vertical mean vs. time-in-fill at each location. The COSY model of the vertical closed orbit evolution during the fill predicts the vertical mean change around the ring. Similarly, `gm2ringsim` can determine the vertical mean change by using internal virtual tracking planes at different azimuthal locations. Figure 12 shows the calorimeter measurements of the vertical mean change from 40 – 300 μs and the corresponding predictions of the two simulation programs. The azimuthal variation in the data supports the implementation of the damaged resistors in the simulation and the projection of the dynamics at all azimuthal locations needed for the phase-acceptance correction discussed in Sec. VII B.

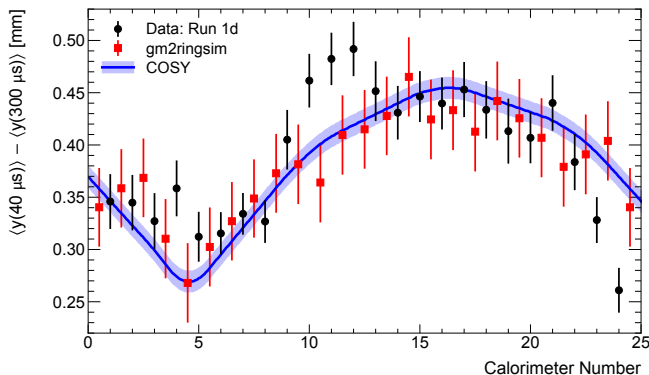


FIG. 12. The change in the vertical mean over the time period from 40 – 300 μs in a fill during Run-1d as measured by the 24 calorimeter stations. The calorimeter data are corrected for acceptance. The blue line corresponds to the COSY model of the vertical closed-orbit evolution during the fill and its prediction of the vertical mean change around the ring. The red squares are from the `gm2ringsim` muon tracking simulation. This implementation of COSY does not utilize beam tracking so the error band is purely systematic, while the `gm2ringsim` errors are statistical. Both simulations have been anchored to data from the tracking station at 270° , and have been shifted azimuthally to align with the maximum acceptance for each calorimeter. The azimuthal structure predicted by the simulations due to the damaged resistors is clearly visible in the data.

VII. MUON LOSS CORRECTION, C_{ml}

Several driving mechanisms can lead to loss of muons during storage. For example, the scattering of particles off of the residual gas in the vacuum chamber, noise from residual high-frequency electromagnetic fields in the system, the sampling of nonlinear fields near the aperture, and nonlinear resonances are potential mechanisms. In Run-1, the muon loss rate was higher than expected owing to a combination of factors including the damaged resistors and the non-optimized kick. However, measure-

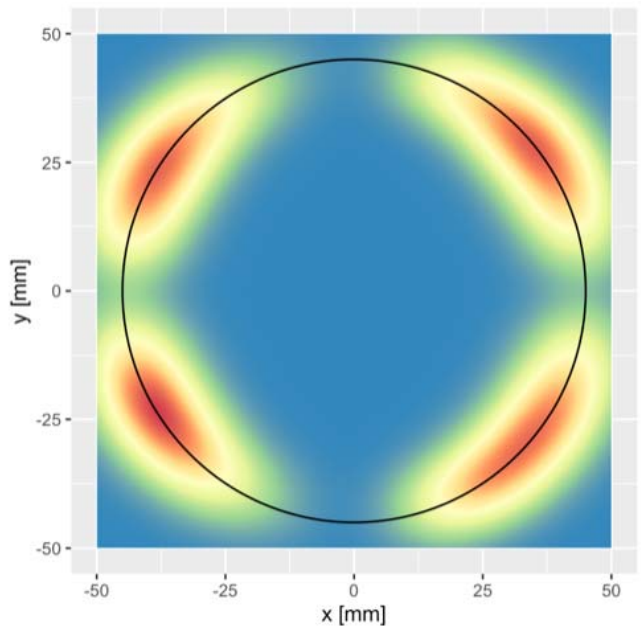


FIG. 13. The intensity distribution of where muons first strike the $r_0 = 45$ mm radius collimators (black circle). For any particular muon, this will occur when its horizontal and vertical betatron oscillations conspire such that the transverse displacement is at r_0 and, at the same time, it is at the azimuthal location in the storage ring of a collimator. Some muons, which will eventually be lost, can survive hundreds to thousands of turns before this condition is met.

ments still show integrated loss rates of less than a percent during the fill.

In general, a muon will be scattered out of the storage region after it strikes one of a set of circular collimated apertures that limit the transverse phase space admittance and its momentum dependence. These collimators have an aperture of radius $r_0 = 45$ mm and are centered on the ideal orbit. Figure 13 shows where on the collimators these muons strike first, a consequence of circular apertures and normal amplitude distributions.

Monte Carlo beamline simulations and simple analytical calculations both predict that a correlation exists between the injected muon average spin phase and the particle momentum. If such a spin-momentum correlation exists, muons that permanently escape from the storage volume during data taking can potentially bias ω_a^m by inducing slow drifts in the phase. The φ_0 fit parameter in Eq. 4 depends on the average initial spin orientation of the muons that produce the detected decay positrons. In this context, an ensemble of muons is said to have a spin-momentum correlation if $d\varphi_0/d\langle p \rangle \neq 0$, where $\langle p \rangle$ is the mean value of the muon momentum for the ensemble of decaying muons that produces the positron spectra being used to measure ω_a^m . The population of stored muons is only depleted by decays, while the population of muons that will be lost is depleted at a faster rate due to decays and losses. The stored and lost muon populations

have different momentum distributions, and so the different rate of depletion creates a time-dependent average of the muon momenta: $d\langle p\rangle/dt \neq 0$. The spin-momentum correlation will combine with the time-dependent muon losses to produce a time-dependent phase:

$$\frac{d\varphi_0}{dt} = \frac{d\varphi_0}{d\langle p\rangle} \frac{d\langle p\rangle}{dt} \neq 0. \quad (19)$$

The three subsections that follow address, in turn, the following topics:

1. The data-driven determination of the absolute rate of muon losses during a fill,
2. The data- and simulation-driven determination of $d\varphi_0/d\langle p\rangle$ at the fit start time, and
3. The data- and simulation-driven determination of the $d\langle p\rangle/dt$ during a fill.

With these rates and correlations in hand, one can evaluate the impact on the muon loss correction factor C_{ml} .

A. Muon loss rate determination

Muons that exit the storage ring during the 30 – 650 μs measuring period deplete the population faster than the expected time-dilated decay $e^{-t/\gamma\tau_\mu}$. The shape of the muon loss function $L(t)$ is accurately measured from the rate of coincident signals in three consecutive calorimeter stations, where each station records an energy deposit of ≈ 170 MeV and the time between stations is ≈ 6.4 ns, corresponding to the energy deposit of a minimum ionizing muon and its time-of-flight between stations, respectively. The muon precession fit includes a term that multiplies the overall normalization N_0 such that

$$N_0 \rightarrow N_0 \Lambda(t) = N_0 \left(1 - K_{loss} \int_0^t e^{t'/\gamma\tau_\mu} L(t') dt' \right). \quad (20)$$

The scale parameter, K_{loss} , can be accurately extracted from the precession analysis to provide the absolute scale of the muon loss function [11]; this is necessary to estimate the phase-related systematic error. We note that the loss function is a property of the beam and should therefore be the same for all calorimeters and energy bins in the precession analyses. An important measure of the rigor of this method is that K_{loss} is independent of which calorimeters are used or which energy bins are selected in the precession fits.

Figure 14 shows the accumulated loss fraction (f_{loss}) for the four data sets in Run-1, defined for $t > t_s$ as

$$f_{loss}(t) = \frac{K_{loss}}{\Lambda(t_s)} \int_{t_s}^t e^{t'/\gamma\tau_\mu} L(t') dt'. \quad (21)$$

This gives the fraction of muons that have been lost from the storage ring with respect to the number present at

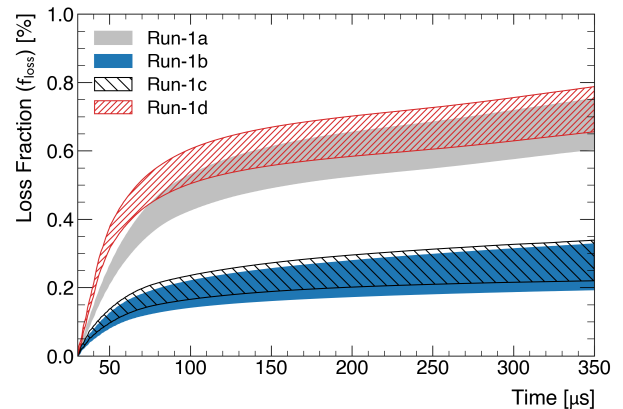


FIG. 14. The integrated fractional muon loss vs. time-in-fill from 30 μs following muon injection. The four curves are from the different run groups. The smaller loss fraction curves are from the $n = 0.120$ data sets (1b, 1c) and the greater loss fractions are from the $n = 0.108$ data sets (1a, 1d). The absolute scale is determined from the K_{loss} parameter following final precession frequency fits. The uncertainty bands on the curves come from two different precession frequency analyses, and whether a small empirical slow correction term to ensure stability of K_{loss} vs. energy is included.

the fit start time. Although all curves rise steeply at early times and gradually at later times, it is clear there are two distinct groups, which are associated with the two different tune n -values (see Table I). We note that the loss fraction in this figure is approximately 8 times larger than the loss fraction measured for Run-2, when the damaged resistors had been replaced. This is strong evidence that the dynamic beam motion during storage led to a high degree of scraping on the collimators at early times, until the beam relaxed to its nominal central value when the voltages had stabilized.

B. Phase-momentum correlation determination

Non-zero spin-momentum correlations, $d\varphi_0/d\langle p\rangle$, are generated in the Muon Campus beamline and muon storage ring. These arise primarily during the circulation of the muons around the Delivery Ring (DR), which is composed of FODO cells and bending dipole magnets. In particular, a dipole bending magnet will change the angle between the muon spin and momentum by $\Delta\varphi \approx a_\mu \gamma \eta_b$, where η_b is the angle at which the muon bends through the dipole field and the momentum dependence is embedded in the γ factor. For k full revolutions of the DR, the angle between the spin and momentum will advance by $\Delta\varphi \approx 2\pi a_\mu \gamma k$, where the sign of phase is defined in the sense that the spin angle precesses with the functional form $\cos(\omega t + \varphi)$. For a hypothetical muon distribution entering the DR with no phase-momentum correlation, the four turns around the DR will imprint a change in φ

of 8.6 mrad per 1% of $\Delta p/p_0$ on the overall distribution. This makes up the majority of the spin-momentum correlation though other smaller contributions are expected from dipole bending magnets in the upstream beamline.

A complete end-to-end simulation has been performed to determine the muon distribution phase space at the exit of the inflector from muons born in all distinct target and beamline regions. The simulation tracks spin and kinematic variables from the production in the target to the delivered beam. A plot of the average phase-momentum correlation from this simulation is shown as the blue band in Fig. 15.

It is possible that this spin-momentum distribution is further perturbed during the storage ring kick because, as illustrated in Fig. 1, the kick does not apply an equal impulse to muons that are distributed longitudinally throughout the incoming bunch. Although this effect appears to introduce a negligible spin-momentum correlation in the simulation, it was possible to perform a direct measurement of the correlation that exists during the measuring period and compare it to the simulation as shown in Fig. 15.

Three special runs were made with the magnetic field of the storage ring set at nominal (1.45 T), reduced (-0.68%), and increased (+0.67%) values. At each setting, an approximately $\pm 0.15\%$ momentum slice of the broad incoming beam is stored, with its central value corresponding to the momentum of the adjusted field settings. The statistical precision on a few hours of beam is sufficient to determine the average spin phase at injection, the precession frequency, and the time-dilated muon lifetime. The values are obtained from fitting the positron vs. time plots to Eq. 3. The change to the precession frequency is proportional to the magnetic field values and readily serves to determine the actual field (and by proxy, momentum) setting. The black points in Fig. 15 show the results of these direct measurements. The fitted slope of (-10.0 ± 1.6) mrad/ $(\% \Delta p/p_0)$ agrees well with the simulation. The error quoted is from the fit alone.

C. Lost-muon momentum correlation determination

A set of special measurements was made to determine the behavior of the muon losses as a function of time-in-fill and momentum. The two damaged resistors were re-inserted into their Run-1 locations during a short period of systematic tests at the beginning of Run-3. One 8-hour period of data collection was acquired in otherwise nominal conditions, to re-establish the Run-1 time-dependence of the CBO frequency, see Sec. VIA, and to provide data that could be used in a COSY simulation of the storage ring behavior under these conditions; see below. The Delivery Ring momentum collimators were used to bias the incoming muon momentum distribution. The collimators can be driven separately on both the high- and low-momentum sides and can traverse the en-

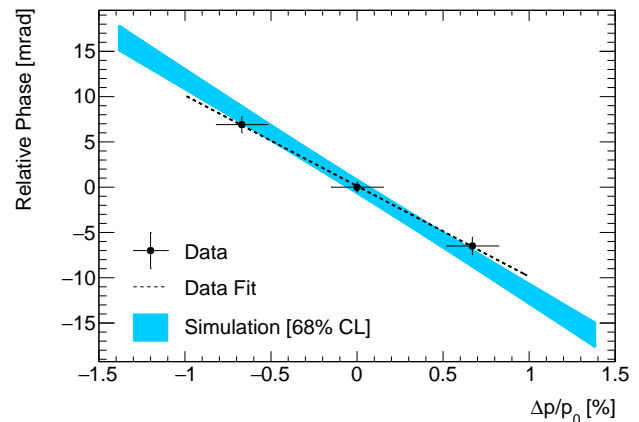


FIG. 15. Phase-momentum correlation from an end-to-end simulation (blue band) and from a data-driven approach (black). The simulation gives the result at the entrance to the storage ring. The three data points are obtained by fits to muon precession frequency data at nominal, reduced, and increased central magnetic field values. The phase reported for these data represented muons stored and fit during the measuring period. The phase dependence on momentum from the data is -10.0 ± 1.6 mrad/ $\% \Delta p/p_0$.

tire horizontal width of the beam.

Figure 16 shows horizontal stored-muon distributions $F_i(x)$ from a subset of these special runs. The dashed line corresponds to the nominal, full-acceptance distribution used for normal data taking. The three colored distributions are from runs where the low, high, or both momentum collimators were used to bias the stored momentum distribution. The fractions in the legend indicate the intensity with respect to the nominal case. For example, a collimator would be moved until the muon storage rate was reduced to that fraction. The muon loss rate vs. time-in-fill was measured for each collimator setting, providing eight distributions (not all shown in the figure) that were used in the analysis below.

An example of the two extremes - 1/5-low (blue) and 1/5-high (red) - correspond to the relative muon loss rates shown in Fig. 17. The low-momentum muons are lost disproportionately early in the fill and the high-momentum muons are lost more often at later times; the other distributions provide intermediate cases.

The eight distributions were used to parameterize an analytical loss-rate function, whose form was motivated by simple simulation phase space studies. Various models were used to assess the reliability of the conclusions from input assumptions. The solid gray curve in Fig. 16 represents a loss rate probability function determined from the integrals of the muon loss vs. time distributions from 30 - 70 μ s. This is simply meant to be illustrative, as the function evolves in shape throughout the fill.

What is needed is a time-dependent muon loss probability function $l(x, t)$, which can be applied to the nominal momentum distribution to yield the time-dependence

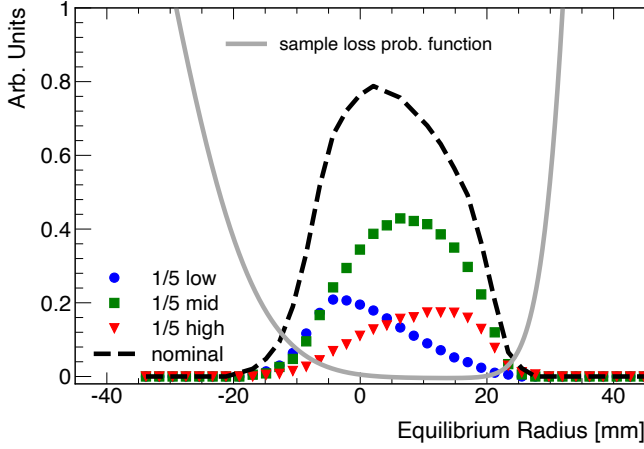


FIG. 16. Four of the eight stored momentum distributions $F_i(x)$ obtained from adjusting the DR high- and low-momentum collimators. The area under each curve is normalized for each DR setting to show the fractional intensity of stored muons with respect to the nominal distribution. The solid gray line is an illustrative muon loss probability function $l(x, t)$ from a model fit to all eight distributions for a time early in the fill. In this time window, the loss probability is greater at low momentum than at high momentum.

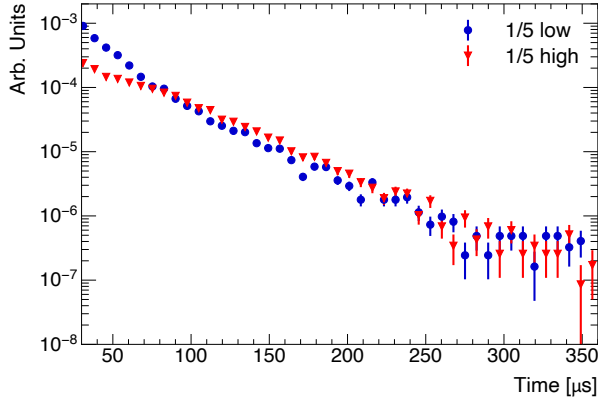


FIG. 17. The muon loss function $L(t)$, normalized to beam intensity, for the lowest (blue) and highest (red) momentum stored momentum distributions; see corresponding momentum distributions in Fig. 16. Asymmetry in the loss rates is seen early in the fill.

of the average momentum of the stored muons. That information is readily translated into a time-dependent spin phase of the stored muons, $\varphi(t)$. The parameters of the function $l(x, t)$ are determined by fitting the eight distributions over increasingly long time ranges from the fit start time $t_s = 30 \mu\text{s}$. At each time t , the fit is performed using eight equations of the form

$$\int_{R_{min}}^{R_{max}} F_i(x) l(x, t) dx = \frac{1}{H_i} \int_{t_s}^t e^{t'/\gamma\tau_\mu} L_i(t') dt', \quad (22)$$

where i runs from 1 to 8 for each of the special runs, and

R_{min} and R_{max} represent the minimum and maximum possible radii of the stored muons; $F_i(x)$ is the measured intensity of the fast rotation distribution for that run as a function of the equilibrium radius, normalized to 1, and $\gamma\tau_\mu \approx 64.4 \mu\text{s}$ is the time-dilated muon lifetime. The empirical loss function $l(x, t)$, which depends on time and radius, is determined in the fit. The measured integrated triples spectrum $L_i(t')$ is integrated from the fit start time to time t . The extra term $e^{t'/\gamma\tau_\mu}$ is included in order to follow the convention of the muon loss term in the decay positron fit function, as expressed in Eq. 20. The normalization by H_i , the total number of positrons measured in that data set, ensures that the eight special runs can be correctly compared.

An analytic form of $l(x, t)$ is assumed in order to perform the fit. From simulations, $l(x, t)$ is expected to peak near the edges of the storage distribution, as muons that have a high or low equilibrium radius are more likely to be lost. Several forms of $l(x, t)$ with this qualitative behavior were compared, including a sum of two Gaussians and a piecewise sum of two parabolas. The same analytic form was used throughout the fill, and the fit parameters were allowed to vary with time to account for the changing behavior of the lost muons.

At each time, the remaining stored distribution $F_{curr}(x, t)$ is calculated using the equation

$$F_{curr}(x, t) = F_0(x) - f_{loss}(t) \frac{F_0(x) l(x, t)}{\int_{R_{min}}^{R_{max}} F_0(x) l(x, t) dx}, \quad (23)$$

where $F_0(x)$ is the fast rotation distribution (see Sec. III) of the full physics data set, normalized to 1, and represents the radial distribution of the stored muons at the fit start. The second term represents the total number of muons that have been lost up to that time, scaled by the fractional loss correction $f_{loss}(t)$, which emerges from the decay positron fit, as seen in Fig. 14.

The average radius of the stored distribution is then extracted at each time from $F_{curr}(x, t)$. This average radius can be converted into momentum units using Eq. 15. The average $\Delta p/p_0$ of the stored distribution is converted to φ using the measured phase-momentum correlation of $(-10 \pm 1.6) \text{ mrad}/(\% \Delta p/p_0)$. The $\varphi(t)$ determined by this method for the four Run-1 data sets, using three different analytical forms of $l(x)$, is shown in Fig. 18; $\varphi(t)$ behaves very similarly, regardless of the form of $l(x)$ used.

D. Value of the muon loss correction

The phase angle $\varphi(t)$ is parameterized using a high-degree polynomial function, which is used to generate a set of points based on the 5-parameter decay positron fit function Eq. 4 with the empirical $\varphi(t)$ inserted. A fit is then performed on the generated points using $\varphi(t) = \varphi_0$, as is assumed in the physics analysis, with all parameters allowed to float. The bias to ω_a^m is extracted by comparing the input ω_a value to the value extracted from fitting

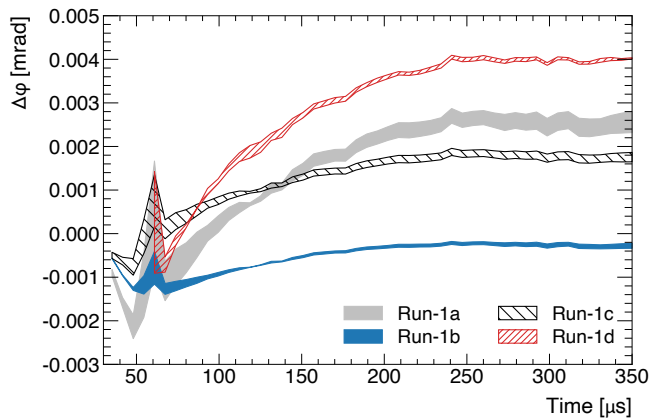


FIG. 18. The expected phase shift versus time-in-fill of the remaining, stored muon population. The uncertainty bands arise from the use of three different $l(x)$ functions.

Data Set	Run-1a	Run-1b	Run-1c	Run-1d
C_{ml}	-14	-3	-7	-17
Phase-momentum	2	0	1	3
Form of $l(t)$	2	0	1	1
f_{loss} function	2	1	2	2
Linear sum ($\sigma_{C_{ml}}$)	6	2	4	6

TABLE VII. Muon loss correction C_{ml} (ppb) with three sources of uncertainty contributing to $\sigma_{C_{ml}}$ (ppb).

with a constant φ . This analysis is repeated for all four data sets.

The correction to ω_a^m from this effect, C_{ml} , is given in Table VII. The muon loss-induced phase change artificially increases the measured value of ω_a^m , so C_{ml} is negative. It varies from -17 to -3 ppb depending on the data set, with Run-1a and Run-1d having larger shifts because of their higher muon loss rates. Three sources of uncertainty are common to all run groups and they are added linearly. The measured phase-momentum correlation of (-10 ± 1.6) mrad/ $(\% \Delta p/p_0)$ contributes a 16% uncertainty ($1 - 3$ ppb). The choice of analytical form of $l(x, t)$ contributes a $0 - 2$ ppb uncertainty. The use of different $f_{loss}(t)$ functions from different analyses contributes $1 - 2$ ppb. To quantify the latter two sources of uncertainty, the full analysis described in the previous section was repeated for every combination of $l(x, t)$ and f_{loss} function. This procedure yields $\sigma(C_{ml}) = 2 - 6$ ppb, which is small on the scale of other Run-1 uncertainties.

VIII. CORRECTION FOR MUON DISTRIBUTION TIME-DEPENDENCE, C_{pa}

The phase of the ω_a oscillation at the moment of a muon's decay is related to the orientation of the muon spin vector relative to its momentum at injection into

the storage ring. The sign of the phase is defined by the convention in Eq. 4 that the positron intensity spectrum modulation is described by a term proportional to $A \cos(\omega_a t + \varphi)$. As discussed in Sec. VII B, the average phase of the incoming polarized muon beam is determined by upstream beamline components and the number of turns in the DR; its value does not affect the extraction of ω_a^m . Ultimately, the observed phase is what a calorimeter detects, an integration of decays from all locations that produce a positron signal in an energy bin E . The phase of the fitted distribution corresponds to the injection phase φ_0 plus any average orientation of the muon spin with respect to its momentum that maximizes the anomalous precession signal.

In Sec. VI A, we described how the calorimeter acceptance is dependent on the transverse decay coordinate. An azimuthally-averaged transverse distribution is shown in Fig. 19. This static image does not convey the radial and vertical oscillations of the mean and width at frequencies associated with the betatron oscillations. They require modification to the normalization, asymmetry, and phase terms in Eq. 4 to fit the spectrum to obtain ω_a^m . The form of these modifications is discussed in [3, 11] and an example form used in our Run-1 ω_a analysis is shown in Appendix D.

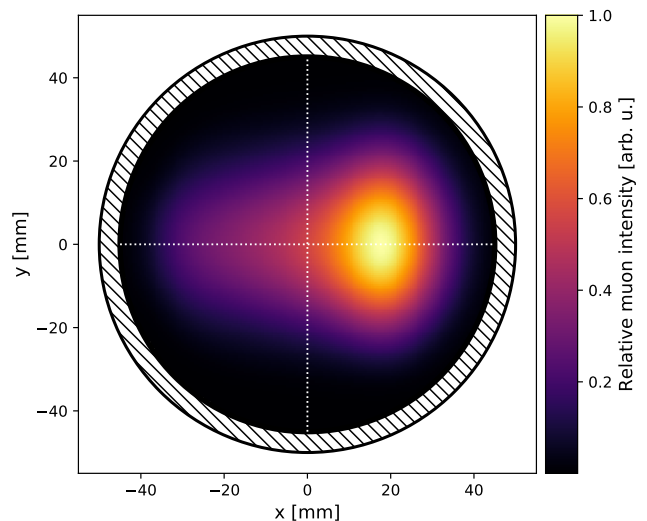


FIG. 19. An azimuthally-averaged muon spatial distribution for Run-1a as measured by the trackers. The (hatched) collimator defines the 45-mm-radius transverse storage aperture.

The phase for a given (x, y) decay coordinate depends on the orientation of the muon's spin that maximizes the acceptance. The 24 calorimeters are finite-sized, placed to the inside of the muon trajectory, and positioned at uniformly spaced azimuthal locations. Therefore the spin orientation of a muon that maximizes acceptance into this system is not parallel to its momentum, but rotated slightly radially inward. This rotation, captured by an effective phase shift φ_{pa} , is a function of transverse decay

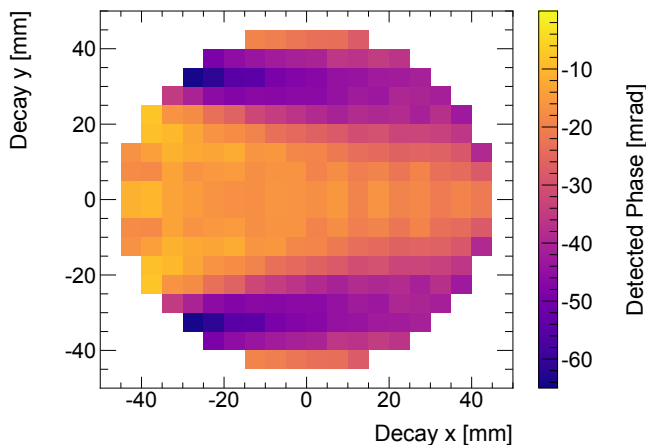


FIG. 20. The azimuthally averaged phase maps for the asymmetry-weighted analysis.

coordinate (x, y) because of acceptance effects. Figure 20 is a “phase map” averaged over azimuth and weighted by the asymmetry-method used to extract ω_a^m from the positron intensity time spectra. The map varies more strongly in the vertical direction, and less so radially. The procedure to create phase maps using `gm2ringsim` is described in Appendix C. Briefly, muon decays are generated over all (x, y, ϕ) coordinates with full muon spin precession vs. time-in-fill properly included. Individual positron intensity spectra from decays originating in a matrix of (x, y) transverse bins are fit to determine ω_a and φ_{xy} . The procedure naturally includes the effects of acceptance and, indeed, acceptance and asymmetry maps are also obtained for each calorimeter.

The spectrum summed across all detectors and all decay coordinates has a modulation frequency ω_a and a net, spatially-averaged phase $(\varphi_0 + \bar{\varphi}_{pa})$. As long as the muon distribution remains constant throughout the measurement period, the net phase is constant. The dependence of the decay-coordinate phase $\varphi_{pa}(x, y)$ on detector acceptance was understood well enough from the E821 experiment to help guide our voltage stability specifications in the development of the new ESQ power-supply network. However, as explained in Sec. VI, the two damaged resistors in Run-1 spoiled the voltage stability requirement on the Q1L upper and lower electrodes, which in turn led to a time-dependence of the mean and width of the muon distribution. In this section, we evaluate how this effect results in a time-dependence of the average coordinate-dependent phase contribution that is not included in the fits to extract ω_a^m from the positron spectrum. A correction factor C_{pa} is needed to correct ω_a^m to the true ω_a needed to determine a_μ .

Figure 21 illustrates how the time-dependence of the muon distribution vertical and horizontal means and widths can lead to an average phase shift $\bar{\varphi}_{pa} \rightarrow \varphi_{pa}(t)$. The exaggerated Gaussian profiles are representative of how such a muon distribution would evolve from early (dotted red) to late (dashed blue) times in a fill. The

average phase $\bar{\varphi}_{pa}$ at any time is calculated by taking a weighted average of the phase values in the map projection, with the weights from the beam intensity (assuming uniform asymmetry and acceptance). The largest effect is from the reduction in the vertical width, where $\bar{\varphi}_{pa}$ is evidently different early compared to late in the fill. In contrast, a small shift of the vertical mean both gains and loses phase nearly symmetrically. The radial phase projection is nearly linear and therefore a mean shift will cause a variation in the phase, whereas a width change is relatively balanced. The radial effects are relatively small and it is the coherent reduction in the vertical width (see Fig. 11b) that dominates the correction to ω_a^m and must be evaluated.

An additional effect that contributes to the phase-acceptance correction has its origin in CBO decoherence. Early in a fill, the betatron oscillations are largely in phase and the beam moves coherently back and forth in the radial direction. When the beam has fully decohered, all calorimeters sample the full radial distribution at once and so the relative acceptance of the full aperture determines the average phase. Conversely, early in the fill when the oscillations are still coherent, the calorimeters sample muon decays from only a subset of the radial distribution at any particular time. In this scenario, the relative acceptance between different radial positions is not important. As a result of this difference between the early and later stages of CBO decoherence, the average phase for an individual calorimeter drifts from early-to-late times in the fill with an impact as large as $\mathcal{O}(100)$ ppb. However, detectors on opposite sides of the ring see the CBO oscillations out of phase with one another, so when considering the sum of the calorimeter data there is a strong cancellation with no net contribution to the C_{pa} correction at a statistically significant level. We do assign an uncertainty owing to the imperfect cancellation of detector pairs that are π radians out of CBO phase. We note that a similar reduction is realized when comparing individual calorimeter positron decay spectra fits to those of the sum. The terms that describe the CBO oscillation amplitudes are 6 – 7 times smaller for the summed spectra compared to fits to individual calorimeters, and the reduction would be more complete if the detector acceptances were identical.

The strategy to evaluate the net phase shift to each of the four data sets in Run-1 involves the following steps:

1. Create high-fidelity maps of acceptance, asymmetry, and phase for each calorimeter (see Appendix C).
2. Determine the time-dependent muon spatial distributions, $M^T(x, y, t)$, for each tracker station T , and for each data set.
3. Evolve those distributions using beam dynamics models and simulations to produce $M^c(x, y, t)$ for all azimuthal locations where calorimeters (c) are placed.

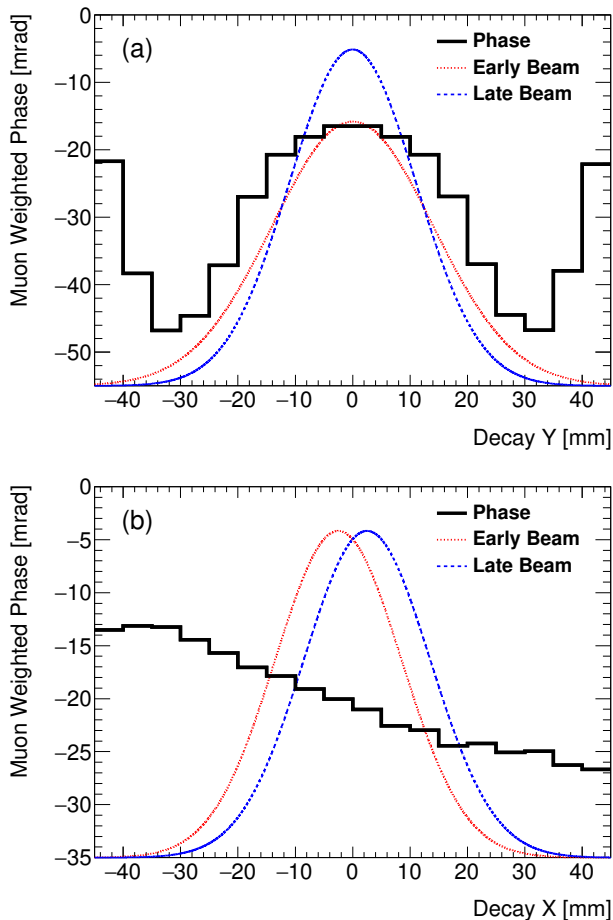


FIG. 21. Phase vs. vertical (a) and horizontal (b) decay coordinate. The Gaussian profiles show (at an exaggerated scale) how muon distributions might evolve from early (dotted red) to late (dashed blue) times in the fill. The largest effect is from the reduction in the vertical width (a), where the phase changes to the distribution add coherently. The mean shift (not shown) is smaller because the increase on one side is balanced on the opposite side. Conversely, the larger phase shift in the radial projection is from the mean motion (b), while the width change (not shown) is largely cancelled.

4. Fold $M^c(x, y, t)$ distributions with acceptance, asymmetry, and phase maps to obtain phase shift vs. time-in-fill for each calorimeter, $\varphi_{pa}^c(t)$.
5. Generate Monte-Carlo data using the full fit function, including the predicted behavior of the phase, $\varphi_{pa}^c(t)$. Fit these pseudo data using the normal fit function to determine the difference in the extracted ω_a^m compared to the input. This difference yields the correction factor C_{pa} for each calorimeter.

A. Measurement of the time-changing muon distribution

The two tracker stations produce the time evolution of the muon distribution maps over the course of a fill, $M^T(x, y, t)$. These distributions are corrected for resolution and acceptance as described in Sec. IID. Betatron oscillations cause the distribution to change rapidly, which makes extraction of the slower terms due to the damaged resistors more difficult. These oscillations are removed from the data by randomizing the time information for each track according to a uniform distribution $U(-T/2, T/2)$ where T is the time period of the oscillation. The modulations at ω_{CBO} , ω_{2CBO} , ω_{VW} , ω_y , and ω_a^m are all removed. This randomization procedure also has the effect of removing the CBO decoherence phase-acceptance effect, which mostly cancels in the sum of all calorimeter data as described above. Figure 11 shows the smooth nature of the vertical projections of the mean $\langle y \rangle$ and width $\sqrt{\langle y^2 \rangle}$ vs. time after the randomization procedure. Naively, one might assume that an average of the two tracker maps will provide the most accurate representation of the muon distribution vs. time and decay coordinates. However, as indicated in Fig. 9, the early-to-late behavior of the storage ring's optical lattice functions varies significantly vs. azimuth because the damaged resistors are located in only one section of the storage ring. The correction is therefore evaluated independently starting from each tracker station and the final result is taken as their average.

B. Estimation of beam distribution around the storage ring

The trackers measure $M^T(x, y, t)$ at two locations around the ring, but the extraction of ω_a^m is performed using calorimeters at 24 azimuthal locations. The damaged resistors were located on the opposite side of the ring with respect to the two tracker positions. This asymmetry leads to differences in the muon transverse distribution measured by the trackers and in the proximity of calorimeters elsewhere in the ring. Both COSY and `gm2ringsim` predict similar relative behavior of $\langle y \rangle(t)$ by azimuthal location, as is shown with a comparison to calorimeter data in Fig. 12. But, the reduction of the vertical width (Fig. 11b) – which cannot be measured by the calorimeters – is more important to the C_{pa} calculation. The $M^T(x, y, t)$ distributions are evolved separately to all azimuthal locations using either the predictions from COSY or `gm2ringsim`. This provides a complete spatial and time distribution of the muons $M^c(x, y, t)$ in the vicinity of a calorimeter based on a measurement at a single point in the ring. The time dependent muon profiles were calculated at an azimuthal angle approximately 22° upstream of each calorimeter's front face, where acceptance is maximal.

Similarly to the treatment for the pitch correction

(Sec. V), the vertical distribution is anchored to the tracker data at its azimuthal location and the distribution at other parts of the storage ring is obtained by scaling the width as a function of azimuth relative to that at the tracker station:

$$y_{\text{pred}}(\phi, t) = y_{\text{tkr}}(t) \frac{y_{\text{pred}}^{\text{RMS}}(\phi, t)}{y_{\text{pred}}^{\text{RMS}}(\phi_{\text{tkr}}, t)}. \quad (24)$$

The width ratio is evaluated directly from virtual tracking planes in `gm2ringsim` and via the ratio of beta functions in `COSY` ($\sqrt{\beta_y(\phi, t)}/\beta_y(\phi_{\text{tkr}}, t)$). From such transformations, vertical beam drifts are properly projected around the ring, and further effects from permanent vertical closed orbit distortions are accounted for in the systematic errors of the correction.

The contribution to C_{pa} from the radial motion of the beam is subdominant, but for a complete treatment the radial beam changes are also included. A similar procedure to that for the vertical changes is followed, although there are added complications due to the interplay of muon momentum and radial position as well as closed-orbit distortions due to azimuthal variation of the main dipole field [10]. Each entry from the measured distribu-

tion is scaled as:

$$x_{\text{pred}}(\phi, t) = \frac{x_{\text{pred}}^{\text{RMS}}(\phi, t)}{x_{\text{pred}}^{\text{RMS}}(\phi_{\text{tkr}}, t)} \cdot (x_{\text{tkr}}(t) - \bar{x}_{\text{tkr}}(t)) + \bar{x}_{\text{pred}}(\phi, t) \quad (25)$$

where the predicted values for $x_{\text{RMS}}(\phi, t)$ and $\bar{x}(\phi, t)$ are taken from tracking planes in `gm2ringsim` and calculated in `COSY` using $\beta_x(\phi, t)$, $D_x(\phi, t)$, and the reconstructed distribution of muon momenta. Measurements of the main dipole storage field are used to calculate the closed orbit distortion included in $\bar{x}_{\text{pred}}(\phi, t)$. After including both vertical and radial manipulations, the procedure has been shown to provide excellent agreement between calculations of C_{pa} using either extrapolated $M^c(x, y, t)$ or beam-tracking planes in a closed-loop simulation test.

C. Phase-acceptance correction: results and uncertainty evaluation

The muon distribution is combined with the simulated maps to extract the time-dependent phase for each calorimeter $\varphi_{pa}^c(t)$ using the following weighted sum:

$$\varphi_{pa}^c(t) = \arctan \frac{\sum_{ij} M^c(x_i, y_j, t) \cdot \varepsilon^c(x_i, y_j) \cdot A^c(x_i, y_j) \cdot \sin(\varphi_{pa}^c(x_i, y_j))}{\sum_{ij} M^c(x_i, y_j, t) \cdot \varepsilon^c(x_i, y_j) \cdot A^c(x_i, y_j) \cdot \cos(\varphi_{pa}^c(x_i, y_j))}. \quad (26)$$

The sum is over all spatial bins. The time-dependence enters via the muon distribution M^c . The acceptance, asymmetry, and phase maps for calorimeter c are represented by ε^c , A^c and φ_{pa}^c . An example evaluation of φ_{pa}^c for the Run-1d data set is shown in Fig. 22. As outlined earlier, the phase increases with time primarily due to the decreasing vertical width of the beam.

The size of the mismeasurement of ω_a^m as a result of the time-dependent phase $\varphi_{pa}^c(t)$ is estimated using simulated data. A histogram is generated for each calorimeter according to the full fit function used to extract ω_a^m , an example of which is described in Appendix D. The spectrum includes betatron oscillations of the normalization, asymmetry, and phase, and a modified $(g-2)$ phase term that has a parameterization of $\varphi_{pa}^c(t)$. The function parameters for each calorimeter are set according to their data-derived values. The resulting simulated data is then fit with the full fit function, but excluding the modified phase term. The difference between the values of ω_a^m that were input and extracted from the fit give the value of the correction C_{pa} for that calorimeter.

The final values correspond to the average of the corrections for all calorimeters, obtained starting from measurements from each of the tracker stations and from performing the procedure using both `COSY` and `gm2ringsim`.

Given that the phase increases with time as shown in Fig. 22, the measured ω_a^m is larger than the true value. The correction C_{pa} must reduce the measured value and is therefore negative. The C_{pa} corrections are shown in Table VIII. The values range from -184 ppb for Run-1a to -117 ppb for Run-1c. The condition of the damaged resistors was worse for the Run-1d data set, which would generally lead to a larger C_{pa} value. In order to keep the correction for Run-1d comparable in size to the other data sets, the fit start time was delayed from 30 to 50 μs , which reduces the correction by a factor of 1.8.

Data Set	Run-1a	Run-1b	Run-1c	Run-1d
C_{pa}	-184	-165	-117	-164
Stat. uncertainty	23	20	15	14
Tracker & CBO	73	43	41	44
Phase maps	52	49	35	46
Beam dynamics	27	30	22	45
Total uncertainty	96	74	60	80

TABLE VIII. Values of the phase-acceptance correction C_{pa} (ppb) and their statistical, systematic, and total uncertainties for each of the Run-1 data sets.

The evaluations of statistical and systematic uncer-

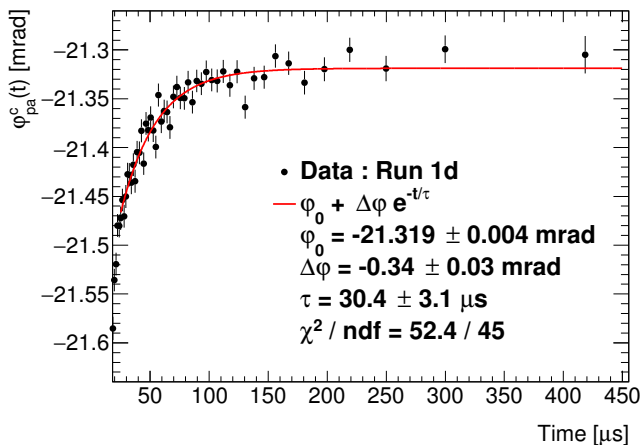


FIG. 22. Calculation of $\varphi_{pa}^c(t)$ for calorimeter 19 in Run-1d using data from the tracker station at 180° and Eq. 26. The fit start time for the extraction of ω_a^m for this data set is 50 μs after injection in order to mitigate the effect of $\varphi_{pa}^c(t)$.

tainty are also detailed in Table VIII. The statistical uncertainty originates from the limited number of tracks available to form $M^T(x, y, t)$ and ranges from 14–23 ppb depending on the size of the data set.

The sources of systematic uncertainty can be grouped into three main areas with no single category dominating over the others. Firstly, there is imperfect knowledge of the tracker’s alignment, resolution, and acceptance corrections, which all affect the measurement of $M^T(x, y, t)$. Uncertainties are estimated by repeating the evaluation of C_{pa} while varying the corrections within a reasonable range based on external constraints. Additionally, there is a statistical tension in Run-1a between the corrections extracted independently from each of the two tracking stations. The uncertainty for this data set is conservatively inflated to account for this. As explained previously, the phase-acceptance effect originating from CBO decoherence will largely cancel when all the calorimeters are summed together. The degree of this cancellation is dependent on the relative amplitudes of the CBO-modulated acceptance oscillation around the ring, which is strongly correlated with the tracker acceptance correction. The uncertainty from the CBO decoherence cancellation is therefore combined linearly with those from the tracker corrections, resulting in values ranging from 41–73 ppb.

Secondly, uncertainties associated with the estimation of the phase, asymmetry, and acceptance maps in Eq. 26 are estimated using the `gm2ringsim` simulation. These uncertainties are dominated by the knowledge of the phase map, which has a much stronger effect on C_{pa} than either the asymmetry or acceptance maps. The possible variation of the map is estimated by comparing measurements of the fitted phase in the actual ω_a^m fits with predictions of φ_{pa}^c from Eq. 26. The time-dependence of

$M^c(x, y, t)$ in the latter is collapsed by taking data from all times in a single time bin. The variation in the final fitted phase as a function of calorimeter number and as a function of calorimeter y -position matches the prediction to within 20%. This variation is used as an estimated uncertainty on the phase map, and the procedure is repeated to propagate this uncertainty to establish a contribution to δC_{pa} . Interactions in material will also affect the detector acceptance and therefore change the phase map (Fig. 29 in Appendix C). The effect of material interactions in the simulation can be exaggerated to allow for quantification of an uncertainty due to mismodeling of material effects. The total uncertainty associated with the map estimation ranges from 46–52 ppb.

Lastly, the procedure utilizes beam dynamics models to extract the calorimeter-specific $M^c(x, y, t)$ distributions from the tracker-measured $M^T(x, y, t)$. Uncertainties are estimated by calculating C_{pa} while varying the beta functions and magnetic fields within constraints from measurements, varying the momentum distribution of the stored muons, and from a comparison between values extracted using either `COSY` or `gm2ringsim`. This uncertainty is smaller than those from the tracker and phase categories in Run-1a, 1b and 1c (22–27 ppb), but is comparable in size in Run-1d (45 ppb). The larger uncertainty in Run-1d is due to the worsening condition of the damaged resistors which increases the azimuthal variation and therefore increases the reliance on the simulations.

Within each group of uncertainties, correlated effects are added linearly and then all remaining effects are summed quadratically to give the total. The total uncertainties (60–96 ppb) range from 45–52% of the correction value.

IX. CONCLUSION

In this paper, we described summaries and conclusions from in-depth studies of four beam dynamics systematic corrections that are required to adjust the measured muon precession frequency ω_a^m (Ref. [11]) to its true physical value ω_a . The corrections for the vertical betatron motion – *pitch* – and the influence of the motional magnetic field on non-magic-momentum muons – *electric field* – are well understood and have been documented by previous generations of $g-2$ experiments. Here, we have refined these studies and performed detailed uncertainty analyses. The pitch correction requires knowledge of the vertical stored muon distribution from the *in situ* tracker system, which provides detailed time-dependent stored-muon spatial profiles in two areas of the storage ring. The electric field correction requires knowledge of the stored muon momentum distribution (alternatively, radial distribution), which is deduced from studying the time evolution of the incoming muon bunch. Two distinct analysis methods are used.

Despite an initial scraping procedure meant to remove

muons that will not remain stored in the ring, a small fraction that will eventually strike a fiducial-defining collimator do survive well into the measurement period. A careful analysis demonstrated that those muons which are lost do not significantly alter the ensemble-averaged spin phase, but we apply a small data-driven correction.

Finally, owing to 2 of 32 damaged high-voltage resistors in the ESQ system that led to slower-than-designed charging times for two plates, the mean and RMS of the stored muon distribution in Run-1 evolved throughout the first $\sim 100 \mu\text{s}$ of the measuring period. Investigation of this effect led to an extensive and new understanding of a subtle coupling of decay coordinate within the storage volume and acceptance vs. spin phase. The coupling to acceptance and phase is carried out by detailed GEANT4-based simulations, and the understanding of the beam motion around the ring through the evolution of the beta functions is simulated in detail using COSY, whose key results are supported by storage simulations using `gm2ringsim`. This “phase-acceptance” effect is time-dependent; its influence on the phase changes rapidly and faster than the muon population decays. Therefore, in the Run-1d period where the resistor time constants were longer than during periods 1a, 1b, and 1c, a fit start-time in the precession fits of $50 \mu\text{s}$ is used to limit the systematic shift to the phase.

A. Summary of Run-1 net corrections to ω_a^m

Table IX presents a summary overview of key findings discussed in this paper. The statistical uncertainty from the asymmetry-weighted analyses of the muon precession data is provided for reference. The four corrections discussed herein are multiplicative adjustments that are applied to convert the raw extracted frequency ω_a^m from the precession fits to the true ω_a value that is needed to determine a_μ as in Eq. 1. The corrections are identified as: electric field C_e , Sec IV; pitch C_p , Sec V; muon-loss-phase C_{ml} , Sec VII; and, phase-acceptance C_{pa} , Sec VIII. Accordingly,

$$a_\mu = \left(\frac{m}{q\tilde{B}} \right) [\omega_a^m \cdot (1 + C_e + C_p + C_{ml} + C_{pa})], \quad (27)$$

where \tilde{B} represents the muon-weighted average magnetic field that is discussed in Ref. [10].

X. ACKNOWLEDGMENTS

We thank the Fermilab management and staff for their strong support of this experiment, as well as the tremendous support from our university and national laboratory engineers, technicians, and workshops.

The Muon $g-2$ Experiment was performed at the Fermi National Accelerator Laboratory, a U.S. Department of Energy, Office of Science, HEP User Facility. Fermilab is managed by Fermi Research Alliance,

	Correction (ppb)	Uncertainty (ppb)
ω_a^m statistical	–	434
C_e	489	53
C_p	180	13
C_{ml}	–11	5
C_{pa}	–158	75
C_{total}	499	93

TABLE IX. The Run-1 combined beam-dynamics corrections to ω_a^m from the four Run-1 data sets. These values are computed with the full correlation matrix formalism used to provide the measured value for ω_a . The values thus reflect fully correlated systematics and weighting from the statistical uncertainties from each data set.

LLC (FRA), acting under Contract No. DE-AC02-07CH11359. Additional support for the experiment was provided by the Department of Energy offices of HEP and NP (USA), the National Science Foundation (USA), the Istituto Nazionale di Fisica Nucleare (Italy), the Science and Technology Facilities Council (UK), the Royal Society (UK), the European Union’s Horizon 2020 research and innovation programme under the Marie Skłodowska-Curie grant agreements No. 690835, No. 734303, the National Natural Science Foundation of China (Grant No. 11975153, 12075151), MSIP, NRF and IBS-R017-D1 (Republic of Korea), the German Research Foundation (DFG) through the Cluster of Excellence PRISMA+ (EXC 2118/1, Project ID 39083149).

Appendix A: Electric Quadrupole Nonlinearity

Consider a 2D projection of the electric field in the ESQ region, as shown in Fig. 23. Laplace’s equation in two dimensions and cartesian coordinates is

$$\nabla^2 V(x, y) = \frac{\partial^2 V}{\partial x^2} + \frac{\partial^2 V}{\partial y^2} = 0. \quad (A1)$$

A potential corresponding to a pure quadrupole field can be written as $V = \frac{1}{2}k(x^2 - y^2)$ for some constant k . The electric field is $E = -\vec{\nabla}V = k(x\hat{x} - y\hat{y})$ with zero divergence, and it is linear in both x and y . Higher-order terms may appear owing to the plate geometry, but the symmetry in the 2D cartesian limit permits only those terms that are odd in x, y . In particular there is no sextupole ($\sim kx^2$) dependence of the field that would be symmetric in displacement.

In the limit of finite curvature, as employed in the storage ring geometry, it is more appropriate to represent the fields in cylindrical coordinates, where Laplace’s equation is

$$\nabla^2 V(\rho, y, \phi) = \left[\frac{1}{\rho} \frac{\partial}{\partial \rho} \left(\rho \frac{\partial}{\partial \rho} \right) + \frac{1}{\rho^2} \frac{\partial^2}{\partial \phi^2} + \frac{\partial^2}{\partial y^2} \right] V = 0, \quad (A2)$$

with $\rho = R_0 + x$. Using the assumption – which is not accurate – that the ESQ system is continuous around the ring so that there is no dependence on the angular coordinate ϕ , the simplest possible solution is

$$V(\rho, y) = \tilde{k} \left[\frac{1}{2} \left(\frac{\rho^2}{R_0^2} - 1 \right) - \ln \frac{\rho}{R_0} - \left(\frac{y}{R_0} \right)^2 \right] \quad (\text{A3})$$

where \tilde{k} is a constant. The electric field is given by

$$\vec{E} = -\vec{\nabla}V = -\frac{\tilde{k}}{R_0^2} \left[\left(\rho - \frac{R_0^2}{\rho} \right) \hat{\rho} - 2y\hat{y} \right] \quad (\text{A4})$$

and expanding in x/R_0 :

$$\vec{E} \approx k \left[\left(x - \frac{x^2}{2R_0} + \dots \right) \hat{\rho} - y\hat{y} \right], \quad (\text{A5})$$

where $k = -2\tilde{k}/R_0^2$. Evidently, Maxwell's equations require a term quadratic in displacement. The quadratic term is equivalent to a sextupole-like component that will affect the chromaticity, complicate the E -field correction, and possibly drive a third order resonance. The general conclusion is that there necessarily exists a symmetric component to the E -field that will contribute to the evaluation of the correction and its systematic uncertainty. This uncertainty is included in Table V as part of the ESQ calibration.

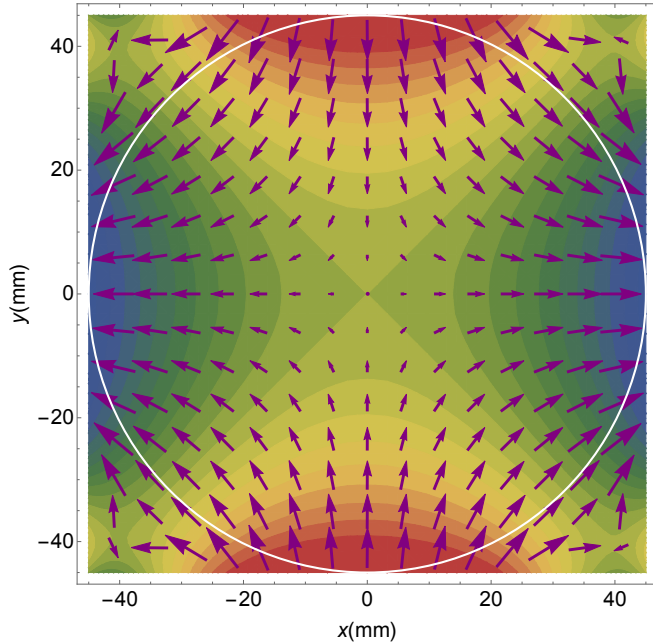


FIG. 23. 2D representation of the equipotentials and electric field in the ESQ region. The circle at radius 45 mm represents the storage ring aperture defined by the collimators.

1. Path length correction owing to curved geometry

The radial electric field along the trajectory of a muon with equilibrium radial offset x_e and betatron amplitude x_β is

$$E_r(s) = k(\eta\delta + x_\beta) - \frac{1}{2R_0}(\eta\delta + x_\beta)^2 + \dots \quad (\text{A6})$$

where $x_e = \eta\delta = \eta \frac{\Delta p}{p}$ and the simple solution above to Laplace's equation is assumed. The average electric field along the trajectory is

$$\langle E_r(s) \rangle = \frac{k}{L} \int_0^L \left(\eta\delta + x_\beta - \frac{1}{2R_0}(\eta\delta + x_\beta)^2 \right) (1 + x_\beta/R_0) ds \quad (\text{A7})$$

where L is the length of the trajectory. Using $x_\beta = x_{\beta 0} \cos \phi(s)$ with $d\phi = \frac{ds}{R_0} = \frac{dl}{(R_0+x)}$, it can be shown that $\langle E_r \rangle$ is approximately

$$\langle E_r(s) \rangle \sim k \left(\eta\delta - \frac{1}{2R_0}((\eta\delta)^2 - \frac{1}{2}x_{\beta 0}^2) + \dots \right) \quad (\text{A8})$$

where $k = n \left(\frac{v_s B}{R_0} \right)$. One observes that the contribution to the average electric field along a trajectory, due to the curvature of the ESQ plates, scales quadratically with the betatron amplitude.

Substitution of Eq A8 into Eq. 13 gives the correction to ω_a due to fractional momentum offset δ and betatron amplitude $x_{\beta 0}$ as

$$\begin{aligned} C_e(\delta, x_{\beta 0}) &\approx -2\delta \frac{\beta k}{cB} \left(\eta\delta - \frac{1}{2R_0}((\eta\delta)^2 - \frac{1}{2}x_{\beta 0}^2) \right) \\ &\approx -2 \frac{\beta k}{cB} \left(\eta\delta^2 - \frac{1}{2R_0}(\eta^2\delta^3 - \frac{1}{2}x_{\beta 0}^2\delta) \right). \end{aligned}$$

The next step requires averaging $C_e(\delta, x_{\beta 0})$ over the entire momentum and CBO distribution.

$$\begin{aligned} \langle C_e(x_e, x_{\beta 0}) \rangle &\approx -2 \frac{\beta k}{cB} \left[\frac{\langle x_e^2 \rangle}{\eta} \right. \\ &\quad \left. - \frac{1}{2R_0} \left(\frac{\langle x_e^3 \rangle}{\eta} - \frac{1}{2} \langle x_{\beta 0}^2 \rangle \frac{\langle x_e \rangle}{\eta} \right) \right] \quad (\text{A9}) \end{aligned}$$

where $\langle \delta \rangle = \langle x_e \rangle / \eta$. If $\langle x_e \rangle / \eta = 0$, and the betatron amplitude and momentum offset are assumed to be uncorrelated, and there is no contribution from the sextupole or path length terms, then

$$\langle C_e(\delta, x_{\beta 0}) \rangle = -2 \frac{\beta k}{cB} \frac{\langle \delta^2 \rangle}{\eta}. \quad (\text{A10})$$

In fact, momentum offset and betatron amplitude are strongly anti-correlated, which will be discussed below. If $\langle x_e \rangle \neq 0$, that is, the muon momentum distribution mean is not centered at the magic momentum, then the

fractional change to the E -field correction from the betatron amplitude consideration is

$$\frac{\langle \Delta C_e(x_e, x_{\beta_0}) \rangle}{\langle C_e \rangle} \sim \frac{-\frac{1}{2R_0} \left[\frac{x_e^3}{\eta} - \frac{1}{2} \frac{\langle x_{\beta_0}^2 \rangle \langle x_e \rangle}{\eta} \right]}{\frac{x_e^2}{\eta}} \\ \sim \frac{-\langle x_e^3 \rangle + \langle x_e \rangle \langle x_{\beta_0}^2 \rangle / 2}{2 \langle x_e^2 \rangle R_0}.$$

For the equilibrium radial distributions typical of Run-1 (see Fig. 6b),

$$\frac{\langle \Delta C_e \rangle}{\langle C_e \rangle} \sim -1.1 \times 10^{-3} + (1.9 \times 10^{-6} \text{mm}^{-2}) \langle x_{\beta_0}^2 \rangle.$$

Conservatively estimating that $\langle x_{\beta_0}^2 \rangle < (45 \text{mm})^2$, the maximum radius of the storage volume, we find that the change in the E -field correction, due to the nonlinearity associated with the curvature of the ESQ plates, is less than 0.5%.

2. Effect from the intrinsic quadrupole nonlinearity

The rectangular cross section of the ESQ geometry introduces a nonlinearity compared to the ideal case. The electric field along the horizontal axis ($y = 0$) can be expressed by

$$E_x - iE_y = (b_n - ia_n) \frac{x^n}{r_0^n} \quad (\text{A11})$$

where $r_0 = 0.045$ m and a_n, b_n are coefficients of the multipoles, which have been fit to an azimuthal slice of a OPERA-3d [27] field map. The fit is for a horizontally pure basis of McMillan functions [43]. Figure 24 shows the horizontal electric field in the midplane, with the evident nonlinear behavior at the extremes. The values from the OPERA map, and from the multipole expansion, are superimposed and are evidently in excellent agreement.

The fitted sextupole-like coefficient can be compared to the estimate discussed previously. A solution satisfying the Laplacian in the curved system was given in Eq. A5. The ratio of the coefficients of the quadratic and linear terms is $r_{hypp} = -\frac{1}{2R_0} = -0.0703 \text{m}^{-1}$, but that hypothetical solution is not unique. Although it satisfies Maxwell's equations, boundary conditions were not yet imposed. The ratio based on the fit to the OPERA field map, that satisfies both Maxwell and the boundary conditions, is $r_{fit} = \frac{b_2}{b_1 r_0} = -2.71281 \times 10^3 / (1.01609 \times 10^6 \times 0.045 \text{m}) = -0.0593 \text{m}^{-1}$, within 16% of our guess.

As was shown above, the effect of the sextupole-like component of the ESQ field, and the asymmetry of the path length about the magic radius, is that the E -field correction depends on betatron amplitude and nonlinearly on equilibrium radial offset. The sextupole-like component and the path-length component contribute with opposite sign, and the amplitude of the sextupole-like component is about 1/2 of the path-length piece.

Based on the measured equilibrium radial distribution, the contribution of the sextupole-like component to the E -field correction is less than 1%. The potential effect from higher-order multipoles was explored in simulation.

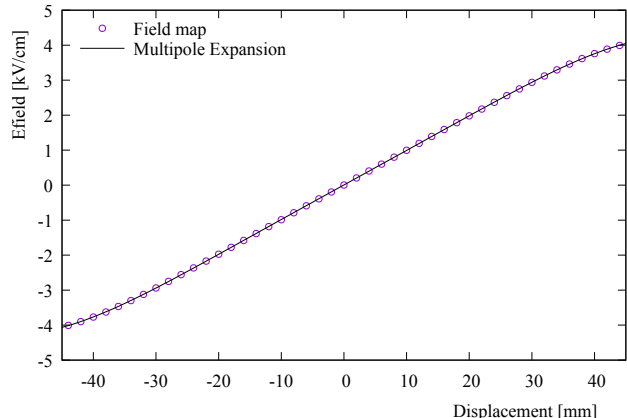


FIG. 24. The electric field along the x -axis in the midplane ($y=0$). The purple points are computed from the multipole expansion using Eq. A11. The black curve uses the values from the field map.

Appendix B: E -field and pitch corrections explored numerically

In simulation ω_a can be determined directly by spin tracking. The trajectory of a muon is established by numerically integrating the equations of motion, and its spin by integration of the BMT equation along that trajectory. In this section the contribution to ω_a due to the electric field and the pitch correction (vertical betatron motion) is explored numerically, in particular to study the nonlinearity that arises from the ESQ geometry, mechanical alignment precision, and high-voltage uncertainty. Spin tracking naturally incorporates the E -field and pitch effects; they cannot be trivially separated.

Full spin tracking verifies to high precision the conclusions for the pitch and E -field corrections as described in Eqs. 17 and 16, respectively. It is, however, computationally intensive. Furthermore, for a trajectory that is both off-momentum and oscillating vertically, spin tracking can not distinguish the contributions from electric field and pitch. In order to explore the full landscape of possible systematic uncertainties, and to understand the contributions from pitch and E -field independently, an efficient and equivalently precise method was developed.

The anomalous precession frequency is commonly ap-

proximated as

$$\vec{\omega}_a = -\frac{q}{m} \left[a_\mu \vec{B} - \left(a_\mu - \frac{1}{\gamma^2 - 1} \right) \frac{\vec{\beta} \times \vec{E}}{c} - a_\mu \left(\frac{\gamma}{\gamma + 1} \right) (\vec{\beta} \cdot \vec{B}) \vec{\beta} \right], \quad (\text{B1})$$

where the experiment actually measures the scalar quantity ω_a^m and not its vector approximation. However, Eq. B1 can be used to produce spin dynamics simulations with short runtimes that allow for the study of a large number of configurations. First, consider the $\vec{\beta} \times \vec{E}$ electric-field term. Define $\Phi_a = \int_0^T \omega_a dt$, there T is the total integrated time that the muon is precessing. In the absence of \vec{E} , Φ_a can be computed by integrating \vec{B}_\perp along the muon trajectory. The contribution from the electric field to ϕ_a is given by

$$\begin{aligned} \frac{\Delta\Phi_E}{\Phi_a} &= \left(a_\mu - \frac{m^2 c^2}{p^2} \right) \frac{1}{c} \int_0^T \vec{\beta} \times \vec{E} dt \\ &\approx -2 \frac{\Delta p}{p} \frac{1}{c} \int_0^T \vec{\beta} \times \vec{E} dt \end{aligned} \quad (\text{B2})$$

where $\Delta p = p - p_0$. In the tracking code it is straightforward to compute the sums in Eq. B2. The electric field correction for the trajectory, assuming that \vec{B} is parallel to $\vec{\beta} \times \vec{E}$, is

$$C_e(T) = -2 \frac{\Delta p}{p} \frac{1}{T} \int^T \frac{\vec{\beta} \times \vec{E}}{Bc} dt. \quad (\text{B3})$$

In a similar manner, the expressions for the pitch correction C_p developed in Sec. V can be rearranged to read

$$C_p(T) = \frac{\Delta\Phi_p}{\Phi_a} = \frac{1}{T} \int^T (1 - |\hat{\beta} \times \hat{\mathbf{B}}|) dt. \quad (\text{B4})$$

To test the equivalence of the shift in precession frequency based on Eqs. B3 and B4, both were computed simultaneously along a single trajectory. The muon is propagated for $1000 \ 2\pi/\omega_a$ in order to determine the spin tune by integrating the Thomas-BMT equation with sufficient accuracy, and $\vec{\beta} \times \vec{E}$ is summed along that same trajectory. The trajectories chosen to test Eq. B3 have momentum offsets but no vertical motion. To test Eq. B4, the tracked muon has magic momentum and zero radial betatron oscillation. The agreement is excellent, as shown in Fig. 25, which shows C_e and C_p for both spin tracking and the integration method.

In the tests of systematics that are described next, the model of the quadrupole field is based on the sum of OPERA-based field maps for each flat ESQ plate, and therefore includes the nonlinearity associated with the geometry, as is evident in Fig. 24. At large amplitudes, the formulas that assume linearity of the electric field slightly overestimate the contributions of the electric field and pitch to ω_a .

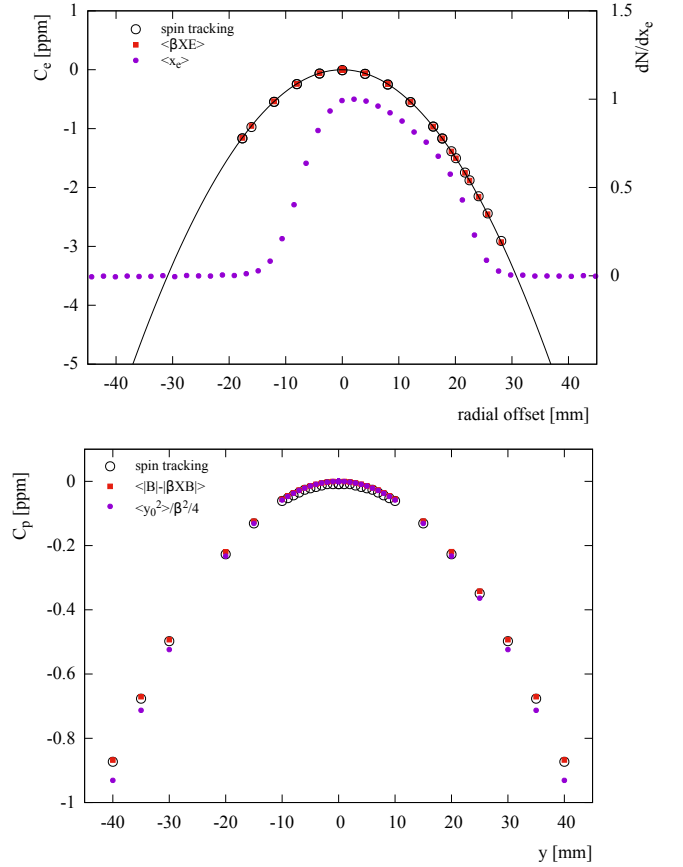


FIG. 25. Top: Contribution to ω_a due to the electric field as computed by spin tracking (integration of the Thomas-BMT equation) and integration along trajectories (Eq. B3) for closed orbits at varying radial offsets. The vertical closed orbit is zero and there is no vertical betatron motion. A representative, measured radial distribution is superimposed for reference. Bottom: Contribution to ω_a due to the vertical oscillation computed with spin tracking and integration along the trajectory (Eq. B4) for muons with magic momentum and zero radial betatron amplitude. Note that the formula that assumes linearity overestimates the contribution at large amplitudes.

The as-built ESQ plate alignment is known with a precision better than ± 1 mm, and the high-voltage set points to $\pm 0.01\%$. To explore the uncertainty from unknown misalignments or voltage errors, 1024 configurations were analyzed, varying the conditions within the specifications. In each case, the E -field and pitch corrections were computed and compared to the reference values. From these studies, a systematic uncertainty of $\sigma(C_p) = 1.3$ ppb is assigned for the contribution from pitching motion due to misalignment and voltage errors. The distribution of perturbations to the electric field correction is not Gaussian and the standard deviation may underestimate the uncertainty. Indeed the error distribution has a strong dependence on the nature of the simulated misalignment and field-error configuration. The systematic uncertainty in the measurement of the contribution from the electric

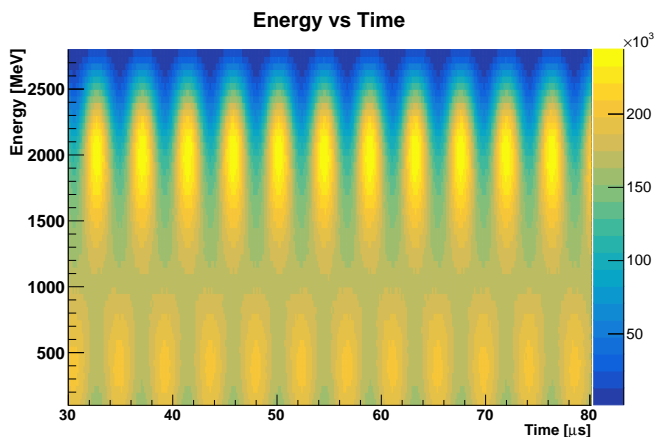


FIG. 26. `gm2ringsim` simulation of detected positron energy as a function of time, with muon decay disabled.

field due to field errors and misalignment is chosen conservatively to be the full width of distribution simulated values, yielding $\sigma(C_e) = 8.7$ ppb.

Appendix C: Maps for the phase-acceptance correction

Estimation of the phase-acceptance correction relies on high-precision maps of detection acceptance, asymmetry, and phase as a function of muon decay coordinate (x, y, ϕ) . In this section, we describe the procedure by which these maps are produced using our `gm2ringsim` GEANT4-based simulation in which all detector systems (calorimeters and trackers), and vacuum chamber hardware of the experiment are fully modeled. The simulation first determines the random time of a muon decay drawn from an exponential distribution. The muon four-momentum, position, and polarization direction are calculated based on the time spent in the storage ring. Finally, the muon is placed at the pre-calculated position and allowed to decay immediately. The orientation of the muon spin at the time of decay is determined from propagating the precession at the ω_a frequency, which is known to sufficient precision from the E821 experiment.

The simulated time and energy distributions of the decay positron match well with the experimental measurement as shown in Fig. 26. This 2D intensity map – with the decaying exponential removed – shows positron energy vs. time-in-fill from 30 – 80 μs . The clear modulations are at the frequency ω_a . The asymmetry reverses around 1 GeV, as expected from the kinematic boost of the Michel spectrum. The simulation does not include CBO modulations because we are only interested in the average detection acceptance effect; the beam dynamic effects that are oscillating at a different frequency are strongly suppressed. Roughly 9 billion muon-decay events are simulated and analyzed to produce maps for three ω_a analysis methods with different positron weight-

ings (see Ref. [11]). In practice, the asymmetry-weighted method provides the most precise determination of ω_a and therefore we will show its maps.

The detection acceptance, asymmetry, and phase maps are produced in the form of 3D histograms $H^c(x, y, E)$ where x and y are the radial and vertical coordinates in the storage ring volume, E is the decay positron energy, and c is a calorimeter index from 1 – 24. For simplicity, we can express these maps as H_{ijk}^c where i and j are x and y coordinates in 5 mm bins, and k is a 50 MeV E bin.

1. Acceptance maps

The average acceptance $\bar{\varepsilon}_{ij}$ for a muon decaying in transverse position bin ij is given by

$$\bar{\varepsilon}_{ij} = \sum_k f_k \varepsilon_{ijk} \sum_{k' > k'_{th}} R_{ijkk'} w_{k'} \quad (\text{C1})$$

where the first sum is over positron truth energy bins k , the second sum is over positron deposited energy bins k' above a threshold k'_{th} , f_k is the fraction of events with energy k , ε_{ijk} is the geometric acceptance for muon decays in bin ij and positron energy k , $R_{ijkk'}$ is the calorimeter response function, and $w_{k'}$ is the analysis weighting factor [11]. $R_{ijkk'}$ represents the probability that a positron in position bin ij and truth energy bin k ends up in the k' detected energy bin. This response function is illustrated in Fig. 27.

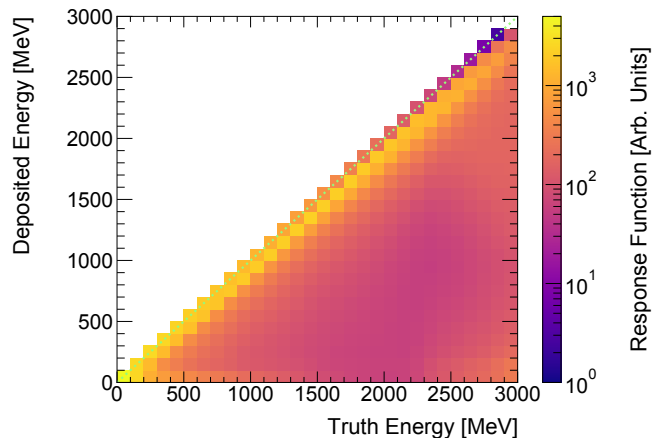


FIG. 27. The average calorimeter response function showing the deposited energy vs. the truth energy, integrated over the decay volume.

Figure 28 shows the relative acceptance function maps for each calorimeter, weighted for the asymmetry-method. The variations among calorimeters are attributed to the material upstream of each, as is shown in Fig. 29. We can loosely identify five categories: 1) behind ESQ plates; 2) behind kicker plates; 3) downstream of the trackers; 4) next to the larger inflector vacuum chamber; and, 5) nothing in front.

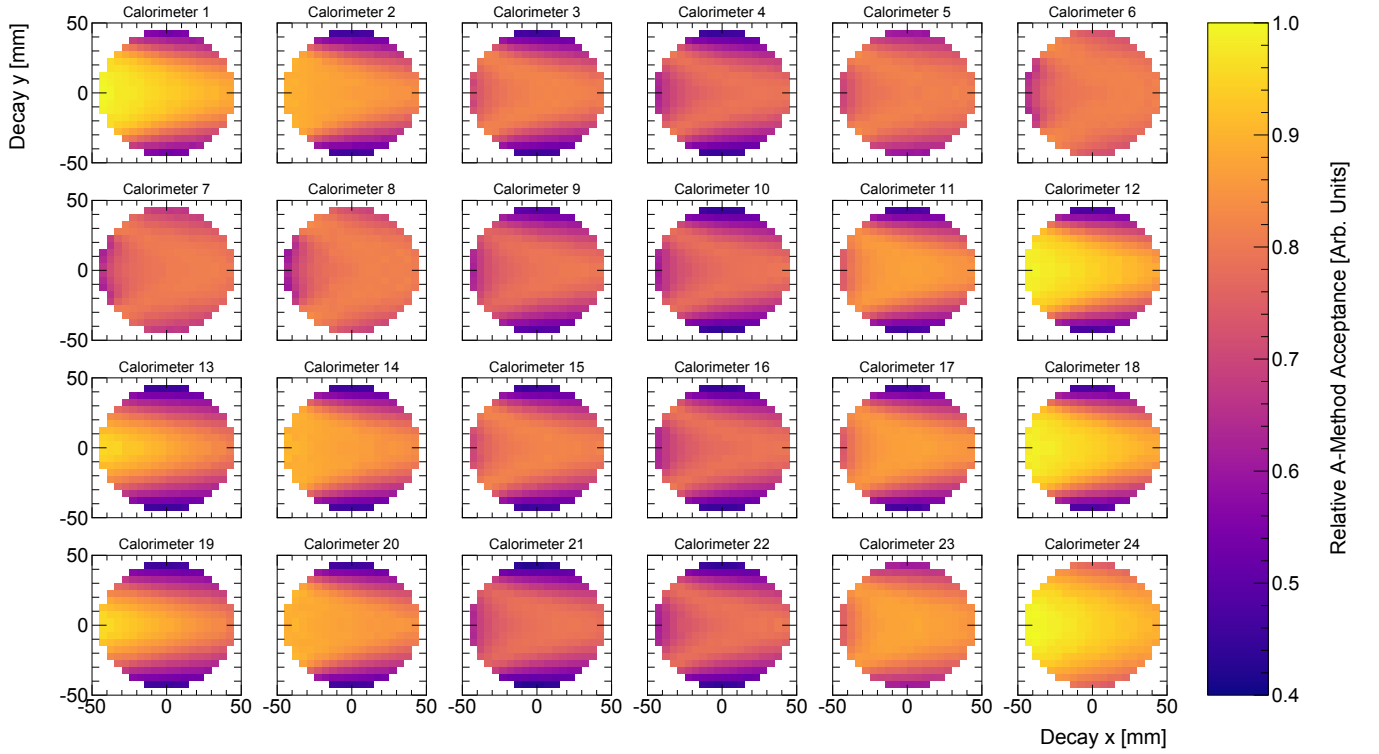


FIG. 28. The asymmetry-weighted relative acceptance maps for all calorimeters. The differences in acceptance derive from the materials just upstream of each station; see Fig. 29.

2. Phase and Asymmetry maps

To produce the asymmetry and phase maps, two types of time spectra are generated: First, a time spectrum for all decay positrons (no matter whether the e^+ is detected or not); and, secondly, a decay $x - y$ grid of time spectra for each detected positron energy bin. Each time spectrum in the ijk -bin is fitted with the five-parameter function $N(t) = N_0 e^{-t/\tau} (1 + A \cos(\omega_a t + \varphi))$, where φ is the fitted phase. The fitted phase for all decay positrons is denoted as φ_0 and the fitted phase for each decay xy bin and energy bin is denoted as φ_{ijk} . The value of each ijk -bin in the phase map is then given by $\varphi_{ijk} - \varphi_0$. Similarly, the value of each ijk -bin in the asymmetry map is given by A_{ijk} .

Figure 29 shows beam-weighted vertical projections of the extracted phase maps. Again, the variation from detector to detector shows a strong dependence on the material in front of the calorimeter. The vertical width changes of the beam couple with the variation in these distributions such that some calorimeters, such as those behind ESQ plates, experience a much larger phase-acceptance effect than those behind the tracker stations.

Appendix D: Precession Fit Function

The complete fit function for the positron arrival time distribution described in Ref. [11] is

$$F(t) = N_0 \cdot N_x(t) \cdot N_y(t) \cdot \Lambda(t) \cdot e^{-t/\gamma\tau_\mu} \cdot [1 + A_0 \cdot A_x(t) \cdot \cos(\omega_a^m t + \varphi_0 \cdot \varphi_x(t))]. \quad (\text{D1})$$

Here, $\Lambda(t)$ is the muon loss function described in Sec. VII A. The terms N_x , N_y , A_x and φ_x describe the interplay between acceptance and beam dynamics that affect the overall calorimeter rate, the average asymmetry and the average phase. They are defined as

$$N_x(t) = 1 + e^{-1t/\tau_{\text{CBO}}} A_{N,x,1,1} \cos(1\omega_{\text{CBO}}t + \varphi_{N,x,1,1}) + e^{-2t/\tau_{\text{CBO}}} A_{N,x,2,2} \cos(2\omega_{\text{CBO}}t + \varphi_{N,x,2,2}), \quad (\text{D2})$$

$$N_y(t) = 1 + e^{-1t/\tau_y} A_{N,y,1,1} \cos(1\omega_y t + \varphi_{N,y,1,1}) + e^{-2t/\tau_y} A_{N,y,2,2} \cos(1\omega_{\text{VW}} t + \varphi_{N,y,2,2}), \quad (\text{D3})$$

$$A_x(t) = 1 + e^{-1t/\tau_{\text{CBO}}} A_{A,x,1,1} \cos(1\omega_{\text{CBO}}t + \varphi_{A,x,1,1}), \quad (\text{D4})$$

$$\varphi_x(t) = 1 + e^{-1t/\tau_{\text{CBO}}} A_{\varphi,x,1,1} \cos(1\omega_{\text{CBO}}t + \varphi_{\varphi,x,1,1}). \quad (\text{D5})$$

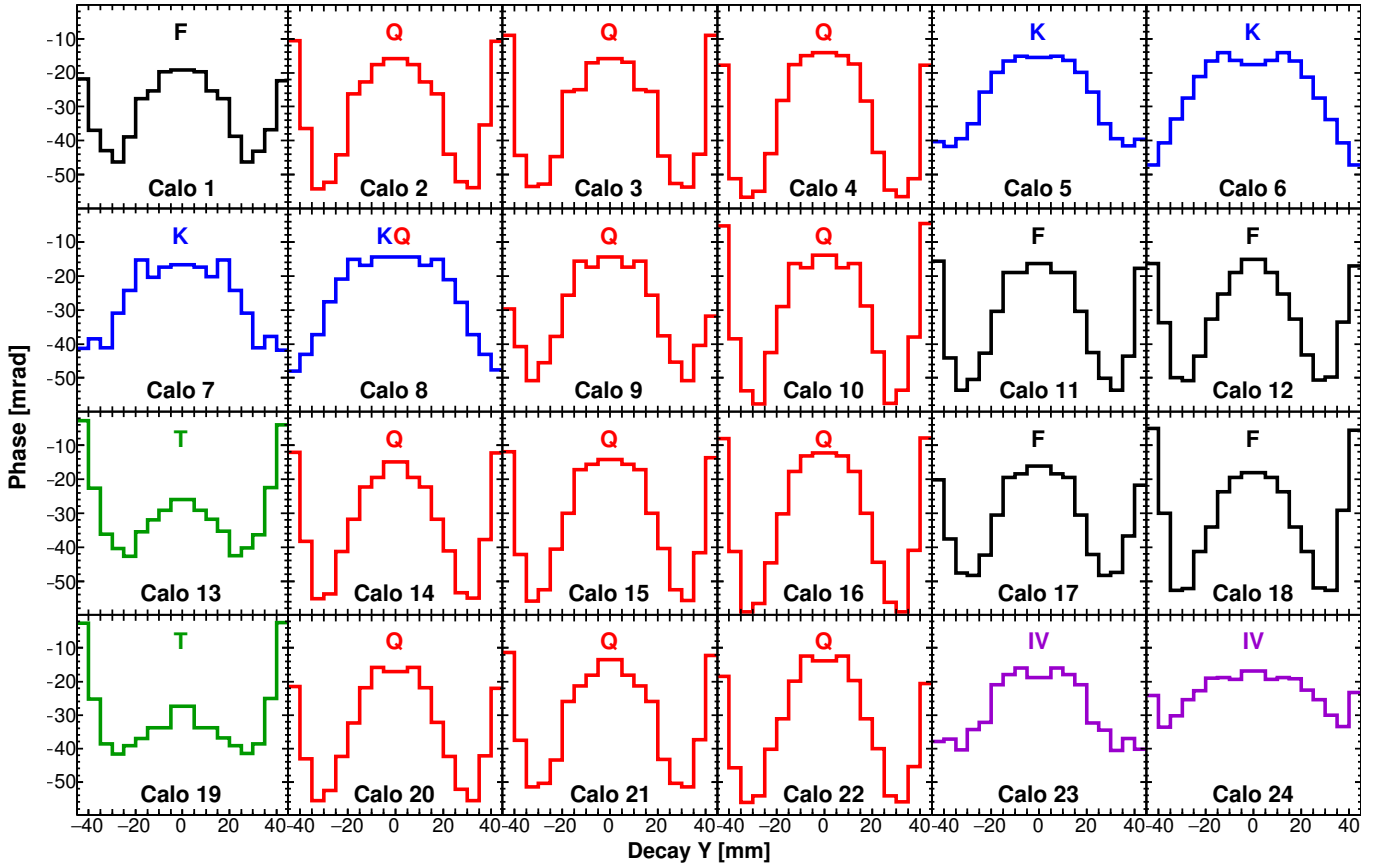


FIG. 29. The asymmetry-weighted vertical projections of the phase maps by calorimeter. The calorimeters are ordered sequentially in azimuth with respect to the injection location. The differences between stations is caused by material differences that impact the transmission of positron decays enroute to detectors. They also impact the acceptance (see Fig. 28) and the phase and asymmetry maps. These indices represent: Q - behind ESQ plates; K - behind kicker plates; T - behind tracker stations; IV - in the constrained inflector vacuum chamber; and, F - free space in front

The parameters of the form $A_{N,x,i,j}$ and $\varphi_{N,x,i,j}$ correspond to the effect of the i^{th} moment of the radial (x) beam distribution at the j^{th} multiple of the relevant fundamental frequency (in this case, ω_{CBO}) on the rate nor-

malization N . Analogous parameters model the modulation of the average asymmetry A and phase φ , as well as the effect of moments of the vertical (y) beam distribution.

-
- [1] J. Bailey, W. Bartl, G. von Bochmann, R. Brown, F. Farley, M. Giesch, H. Jostlein, S. van der Meer, E. Picasso, and R. Williams, Precise Measurement of the Anomalous Magnetic Moment of the Muon, *Nuovo Cim. A* **9**, 369 (1972).
- [2] J. Bailey *et al.* (CERN-Mainz-Daresbury), Final Report on the CERN Muon Storage Ring Including the Anomalous Magnetic Moment and the Electric Dipole Moment of the Muon, and a Direct Test of Relativistic Time Dilation, *Nucl. Phys.* **B150**, 1 (1979).
- [3] G. Bennett *et al.* (Muon G-2 Collaboration), Final Report of the Muon E821 Anomalous Magnetic Moment Measurement at BNL, *Phys.Rev.* **D73**, 072003 (2006), [arXiv:hep-ex/0602035](https://arxiv.org/abs/hep-ex/0602035) [hep-ex].
- [4] T. Aoyama *et al.*, The anomalous magnetic moment of the muon in the Standard Model, *Phys. Rept.* **887**, 1 (2020), [arXiv:2006.04822](https://arxiv.org/abs/2006.04822) [hep-ph].
- [5] W. D. Phillips, W. E. Cooke, and D. Kleppner, Magnetic moment of the proton in H₂O in bohr magnetons, *Metrologia* **13**, 179 (1977).
- [6] E. Tiesinga, P. J. Mohr, D. B. Newell, and B. N. Taylor, The 2018 CODATA Recommended Values of the Fundamental Physical Constants (Web Version 8.1), <http://physics.nist.gov/constants>.
- [7] W. Liu *et al.*, High precision measurements of the ground state hyperfine structure interval of muonium and of the muon magnetic moment, *Phys. Rev. Lett.* **82**, 711 (1999).
- [8] D. Hanneke, S. F. Hoogerheide, and G. Gabrielse, Cavity Control of a Single-Electron Quantum Cyclotron: Measuring the Electron Magnetic Moment, *Phys. Rev. A* **83**, 052122 (2011), [arXiv:1009.4831](https://arxiv.org/abs/1009.4831) [physics.atom-ph].
- [9] B. Abi *et al.* (Muon $g-2$), Measurement of the Positive

- Muon Anomalous Magnetic Moment to 0.46 ppm, *Phys. Rev. Lett.* **126**, 141801 (2021).
- [10] T. Albahri *et al.* (Muon $g-2$), Magnetic Field Analysis for the Muon $g-2$ Experiment at Fermilab, *Phys. Rev. A* **103**, 042208 (2021).
- [11] T. Albahri *et al.* (Muon $g-2$), Measurement of the anomalous precession frequency of the muon in the Fermilab Muon $g-2$ experiment, *Phys. Rev. D* **103**, 072002 (2021).
- [12] V. Bargmann, L. Michel, and V. Telegdi, Precession of the polarization of particles moving in a homogeneous electromagnetic field, *Phys. Rev. Lett.* **2**, 435 (1959).
- [13] J. D. Jackson, *Classical Electrodynamics*, 3rd ed. (Wiley, New York, NY, 1999).
- [14] G. Bennett *et al.* (Muon (g-2) Collaboration), An Improved Limit on the Muon Electric Dipole Moment, *Phys. Rev. D* **80**, 052008 (2009), arXiv:0811.1207 [hep-ex].
- [15] D. Stratakis, B. Drendel, J. P. Morgan, M. J. Syphers, and N. S. Froemming, Commissioning and First Results of the Fermilab Muon Campus, *Phys. Rev. Accel. Beams* **22**, 011001 (2019).
- [16] G. T. Danby *et al.*, The Brookhaven muon storage ring magnet, *Nucl. Instrum. Meth.* **A457**, 151 (2001).
- [17] R. Prigl, U. Haeberlen, K. Jungmann, G. zu Putlitz, and P. von Walter, A high precision magnetometer based on pulsed NMR, *Nucl. Instrum. Meth.* **A374**, 118 (1996).
- [18] A. Yamamoto *et al.*, The superconducting inflector for the BNL g-2 experiment, *Nucl. Instrum. Meth.* **A491**, 23 (2002).
- [19] Y. K. Semertzidis *et al.*, The Brookhaven muon (g-2) storage ring high voltage quadrupoles, *Nucl. Instrum. Meth.* **A503**, 458 (2003).
- [20] K. S. Khaw *et al.* (Muon g-2), Performance of the Muon $g-2$ calorimeter and readout systems measured with test beam data, *Nucl. Instrum. Meth.* **A945**, 162558 (2019), arXiv:1905.04407 [physics.ins-det].
- [21] J. Kaspar *et al.*, Design and performance of SiPM-based readout of PbF₂ crystals for high-rate, precision timing applications, *JINST* **12** (01), P01009, arXiv:1611.03180 [physics.ins-det].
- [22] A. Anastasi *et al.* (Muon g-2), The laser-based gain monitoring system of the calorimeters in the Muon $g-2$ experiment at Fermilab, *JINST* **14**, P11025, arXiv:1906.08432 [physics.ins-det].
- [23] E. M. Metodiev *et al.*, Analytical Benchmarks for Precision Particle Tracking in Electric and Magnetic Rings, *Nucl. Instrum. Meth. A* **797**, 311 (2015), arXiv:1503.02247 [physics.acc-ph].
- [24] T. Arvanitis and A. Lyon, artG4: A Generic Framework for Geant4 Simulations, *J. Phys. Conf. Ser.* **513**, 022023 (2014).
- [25] S. Agostinelli *et al.* (GEANT4), GEANT4: A Simulation toolkit, *Nucl. Instrum. Meth. A* **506**, 250 (2003).
- [26] C. M. Poole, I. Cornelius, J. V. Trapp, and C. M. Langton, A CAD Interface for GEANT4, *Australasian Physical & Engineering Science in Medicine* [10.1007/s13246-012-0159-8](https://doi.org/10.1007/s13246-012-0159-8) (2012).
- [27] *OPERA-3d User Guide* (Vector Fields Limited, Oxford, England, 2004).
- [28] D. A. Tarazona, M. Berz, and K. Makino, Muon loss rates from betatron resonances at the Muon $g-2$ Storage Ring at Fermilab, *Int. J. Mod. Phys. A* **34**, 1942008 (2019).
- [29] K. Makino and M. Berz, COSY INFINITY Version 9, *Nucl. Instrum. Meth. A* **558**, 346 (2006).
- [30] E. Valetov, M. Berz, and K. Makino, Computation of the Main and Fringe Fields for the Electrostatic Quadrupoles of the Muon $g-2$ Storage Ring, *Int. J. Mod. Phys. A* **34**, 1942041 (2019).
- [31] I. Engineering Software, *COULOMB*, <https://www.integratedsoft.com/product/coulomb/>.
- [32] M. Berz, *Modern Map Methods in Particle Beam Physics* (Academic Press, 1999).
- [33] D. Sagan, Bmad: A relativistic charged particle simulation library, *Nucl. Instrum. Meth. A* **558**, 356 (2006).
- [34] Y. Orlov *et al.*, Muon revolution frequency distribution from a partial-time Fourier transform of the $g-2$ signal in the muon $g-2$ experiment, *Nucl. Instrum. Meth.* **A482**, 767 (2002).
- [35] F. Combley and E. Picasso, The Muon (G-2) Precession Experiments: Past, Present and Future, *Phys. Rept.* **14**, 1 (1974).
- [36] F. J. M. Farley and Y. K. Semertzidis, The 47 years of muon $g-2$, *Prog. Part. Nucl. Phys.* **52**, 1 (2004).
- [37] J. P. Miller, E. de Rafael, B. L. Roberts, and D. Stöckinger, Muon (g-2): Experiment and Theory, *Ann. Rev. Nucl. Part. Sci.* **62**, 237 (2012).
- [38] G. W. Bennett *et al.* (Muon g-2), Statistical equations and methods applied to the precision muon (g-2) experiment at BNL, *Nucl. Instrum. Meth. A* **579**, 1096 (2007).
- [39] F. J. M. Farley, Pitch correction in (g-2) experiments, *Phys. Lett.* **B42**, 66 (1972).
- [40] F. J. M. Farley and E. Picasso, The Muon g-2 experiments, *Adv. Ser. Direct. High Energy Phys.* **7**, 479 (1990), [479(1990)].
- [41] J. H. Field and G. Fiorentini, Corrections to the $g-2$ frequency in weak focusing storage devices due to betatron oscillations, *Nuovo Cim. A* **21**, 297 (1974).
- [42] A. J. Silenko, Equation of spin motion in storage rings in the cylindrical coordinate system, *Physical Review Special Topics - Accelerators and Beams* **9**, [10.1103/physrevstab.9.034003](https://doi.org/10.1103/physrevstab.9.034003) (2006).
- [43] E. M. McMillan, Multipoles in Cylindrical Coordinates, *Nucl. Instrum. Meth.* **127**, 471 (1975).